Prediction of Entrained Droplet Fraction in Co-Current Annular Gas–Liquid Flow in Vertical Pipes

Aliyu M. Aliyu[1], Almabrok A. Almabrok[2], Yahaya D. Baba[3], Archibong Archibong-Eso[4], Liyun Lao[4], Hoi Yeung[4], Kyung Chun Kim[1*]

[1]School of Mechanical Engineering, Pusan National University, 609-735 Busan, Republic of Korea
[2]Department of Petroleum Engineering, Faculty of Engineering, Sirte University, Sirte, Libya
[3]Department of Chemical and Petroleum Engineering, Afe Babalola University, PMB 5454, Nigeria
[4]Oil and Gas Engineering Centre, Cranfield University, Bedfordshire MK43 0AL, United Kingdom

*Corresponding author
E-mail address: kckim@pusan.ac.kr (K.C. Kim)

Abstract

The entrained droplet fraction is an important parameter in annular two-phase flow, as its correlations are key inputs in flow simulation codes for the prediction of pressure drop and critical heat flux or dryout. Investigators have stressed the importance of extending the validity range of current correlations so that more conditions are covered. This could be achieved for example by including fluids with higher viscosities, a wider range of operating pressures, and increase in the size of pipes used for experiments (most of the data in the literature are from pipes of 50 mm diameter and below). In attempt to improve the latter, experiments were conducted in a 101.6 mm gas–liquid flow loop at Cranfield University's Oil and Gas Engineering Laboratory and data on the fraction of droplets were collected in the annular flow regime by measuring the film velocity, from which the droplet fraction was calculated. Comparison of the film velocity by this method and by a mass balance showed close agreement. A capacitance Wire Mesh Sensor was used for flow visualisation in order to distinguish between annular and churn flow. In order to arrive at an improved correlation, over 1,300 data points were gathered from other published works. These include air–water studies where large pipes of up to 127 mm in diameter were used. The others were from small-diameter pipes and for refrigerant, steam–water, air–water, and air–glycerine flows. Since in the annular regime, the gas flow entrains liquid droplets into the core, their presence alters the properties of the gas core. Therefore, accurate predictions are pivotal for the energy efficient design and operation of facilities in the petroleum and nuclear power industry. The correlation obtained here showed good agreement with the collected databank.

Keywords: droplet entrainment, large diameter pipes, two-phase flow, Sauter mean diameter, Wire Mesh Sensor.

Nomenclature

A. Roman		
A	[m^2]	Cross-sectional area
D	[m]	Pipe internal diameter
d_{32}	[m]	Sauter mean diameter
e	[-]	Entrained liquid fraction
Fr	[-]	Froude number
g	[m/s^2]	Acceleration due to gravity
G	[kg/m^2-s]	Total liquid mass flux
h_{LG}	[J/kg]	Specific latent heat of vaporisation
L	[m]	Pipe length
$\dot{m}$	[kg/s]	Phase mass flow rate
N_μ	[-]	Viscosity number
P	[Pa]	Local pressure
$\dot{q}$	[W/m^2]	Heat flux through pipe wall
R	[kg/s]	Rate of droplet deposition or entrainment
Re	[-]	Reynolds number
t	[m]	Film thickness
u	[m/s]	Phase superficial velocity
We	[-]	Weber number
x	[-]	Gas quality
B. Greek		
$\bar{\delta}$	[m]	Average height of disturbance waves
ε	[-]	Void fraction
γ	[-]	Liquid droplet hold up
ν	m^2/s	Kinematic viscosity
μ	[kg/s-m]	Dynamic viscosity
ρ	[kg/m^3]	Density
σ	[N/m]	Liquid surface tension
C. Subscripts		
c	Core	
dep	Deposition (subscript for *R*)	
ent	Entrainment (subscript for *R*)	
g	Gas phase	
l	Liquid phase	
lf	Liquid film	
sg	Superficial gas	
sl	Superficial liquid	

1 Introduction

Annular flow is one of the most commonly observed flow regimes and occurs in industrial applications involving gas–liquid flows. These include air conditioning, heat exchangers, wet gas

pipelines and also in nuclear power plants such boiling and pressurised-water reactors (BWRs and PWRs). In the former, such conditions are encountered in the core during normal operation while for the latter case, in the steam generators and in the upper-core components during normal operation and in the reactor during off-normal conditions, including accident occurrences [1]. This flow pattern is characterised by a continuous liquid film flowing along the pipe's inner circumference and a centralised gas core containing liquid droplets entrained from the flowing liquid film. Accurate modelling of the amount of liquid entrained in the gas core (the entrained droplet fraction) is important for correctly estimating pressure drop and pumping requirements in pipes. It is also essential for the appropriate design of downstream oil and gas facilities, predicting the inception of dry-out or critical heat flux (CHF) in boiling heat transfer, and the efficiency of nuclear reactor core cooling. High gas qualities favour high levels of droplet entrainment. When the fraction of droplets entrained approach unity, the liquid film thickness/flow rate approach zero, and CHF flux sets out. The flow pattern then transitions from annular–mist to mist flow. At this transition point, it has been shown [2] that the slope of the pressure gradient plot against gas flow rate changes sign. Therefore, accurate knowledge of the entrained droplet fraction is of paramount importance in predicting and avoiding the incidence of CHF during operation, hence averting damage to equipment, which can carry huge economic and safety implications. Indeed as was pointed out by Hewitt and Hall-Taylor [3], a triangular inter-relationship exists between the liquid film flow rate (hence entrained droplet flow rate), film thickness, and pressure gradient (or shear stress). This makes rigorous analytical/numerical modelling and prediction difficult, thus necessitating the use of closure relationships (correlations) for either the film thickness, or entrained droplet fraction. Closure relationships for the entrained liquid in a gas flow are usually empirical or semi-empirical correlations. They are embedded in thermal-hydraulic codes and these are executed in each simulation iteration.

Correlations for the entrained droplet fraction have been obtained over the years by many investigators, with a majority using air and water as the working fluids in their experiments [4]–[11]. Nonetheless, these studies were conducted using tubes of internal diameter (ID) between 5 and 60 mm. These are smaller than typical wet gas risers, for example, where the tubes have diameters of at least 200 mm. Many authors who have cautioned about extrapolating multiphase flow parameters (such as liquid film thickness, two-phase/interfacial friction factor, or droplet fraction) from small ($D < 100$ mm) to large-diameter ($D \geq 100$ mm) pipes, as is done for single-phase flows [6], [12]–[14].

Therefore, the purpose of this study is to determine the suitability of published correlations for the prediction of entrained droplet fraction in large pipes and small pipes where the flow conditions and test fluids are different. We also propose a correlation obtained using an extensive database that includes entrained fractions obtained from large-diameter pipes for the first time. To achieve this, we use data collected from Cranfield University's 101.6-mm Serpent Rig flow facility along with other

data from 125 and 127-mm ID risers. Liquid film velocity measurements were used to calculate the droplet entrainment fraction, and flow visualisation techniques with a capacitance wire mesh sensor (WMS) were used alongside visual observations to properly identify flow regimes.

2 Entrainment mechanisms

A distinctive feature of annular two-phase flow is the complex pattern of gas–liquid interfacial waves, which manifest as so-called "disturbance waves" in certain flow conditions. These disturbance waves have long been considered a source of entrained droplets, but the behaviour is still not fully understood. Based on visual observations, several mechanisms have been proposed [3], including disturbance wave breakdown by "undercutting", "rolling", and bubble breakup. In Figure 1a, flowing gas undercuts the wave such that a round liquid bead begins to form. The neck of the developed bead elongates to a point where it breaks up into droplets.

Droplet entrainment by roll wave breakup occurs when a large disturbance wave on a shallow liquid film becomes steep along the gas flow direction and forms a tip that breaks up into droplets, as shown in Figure 1b. Liquid breakup leading to entrainment may also occur from a release of bubbles at the gas–liquid interface (Figure 1c). Garner et al. [15] and Newitt et al. [16] did pioneering work on this phenomenon and found that bubble breakup can occur in one of two ways: gas jet breakdown for small bubbles and bubble collapse for larger bubbles. Low surface tension and liquid viscosity give rise to smaller bubbles. Wetting agents can reduce the amount liquid droplets entrained by bubble breakup and the production of smaller droplets.

Lastly, droplet entrainment by liquid impingement occurs when large liquid droplets impinge on the surface of the liquid interface, resulting in further entrainment of lesser droplets (Figure 1d). Kuo and Cheung [17] note that an advancing roll wave may also cause the production of smaller droplets by impingement. These entrainment mechanisms lead to a decrease in disturbance wave amplitude as the gas flow increases, resulting in a reduction in the liquid film thickness as the droplets are entrained. For a given gas flux, droplet deposition occurs from the gas core to the liquid film, and a dynamic equilibrium is established between droplet entrainment and deposition, hence keeping the liquid film flow rate fairly constant at specified conditions. This is described by [7], [18]:

$$\frac{d\dot{m}_{lf}}{dL} = \frac{4}{D}(R_{dep} - R_{ent} - \dot{q}/h_{LG}) \qquad (1)$$

where R_{dep} and R_{ent}, L, $\dot{q}$ and h_{LG} are the mass flow rates of deposition, mass flow rate of entrainment, axial distance along the pipe, heat flux through pipe wall, and specific latent heat of vaporisation respectively. At equilibrium, where $R_{dep} = R_{ent}$, and no heat addition, $d\dot{m}_{lf}/dL = 0$ and the liquid film flow rate, hence film thickness becomes constant.

3 Criteria for droplet entrainment onset

The onset or inception of droplet entrainment is the point at which the first liquid droplet tears from the surface of the liquid after a small change in gas or liquid flow rate [3]. When the gas phase flows over the liquid film, the interface becomes unstable with increasing gas velocity due to Kelvin-Helmholtz instability. At adequately high gas flow rates, these interfacial waves transition into large-amplitude disturbance waves. A point reaches where the shear forces at the gas–liquid interface dominate the competing surface tension forces within the liquid, culminating in droplets tearing off and entraining in the highly turbulent gas flow. The Weber number is widely used to study this phenomenon since it expresses these competing forces:

$$We = \frac{\rho u^2 D}{\sigma} \tag{2}$$

The Weber number is particularly useful when strongly curved surfaces are involved, such as in pipes [19]. Wicks and Duckler [20] experimental observations show that a critical Weber number (We_{cr}) of 22 is required for the inception of droplet entrainment. They developed a correlation based on the Martinelli parameter X and We_{cr}, which Ishii and Mishima [21] noted that it had reasonable agreement with experimental data but limited applicability due to its dimensional nature. Ishii and Grolmes [22] studied the onset of entrainment, reporting a critical liquid Reynolds number ($Re_{l,cr}$) of 160 for horizontal and vertical upflow. By making a force balance on the crest of a hypothetical liquid roll wave, they proposed an inception criterion as follows:

$$\frac{\mu_l u_{sg}}{\sigma}\sqrt{\left(\frac{\rho_g}{\rho_l}\right)} \geq 11.78 N_\mu^{0.8} Re_l^{-1/3} \textbf{ for } N_\mu \leq 1/15 \tag{3}$$

and

$$\frac{\mu_l u_{sg}}{\sigma}\sqrt{\left(\frac{\rho_g}{\rho_l}\right)} \geq 1.35 Re_l^{-1/3} \textbf{ for } N_\mu > 1/15 \tag{4}$$

where the viscosity number N_μ is defined as

$$N_\mu = \mu_l / \left(\rho_l \sigma \sqrt{\sigma / g\Delta\rho}\right)^{1/2} \tag{5}$$

while the superficial liquid Reynolds number is defined as

$$Re_l = \frac{\rho_l u_{sg} D}{\mu_l} \tag{6}$$

A point called the "rough turbulent" regime is reached at $Re_l \leq 1635$, where the critical gas Reynolds number is independent of the liquid Reynolds number. Ishii and Mishima (1989) noted a good fit with experimental data and significant scatter around the criterion. They argued that since there are many droplets along the interface, the gas core inertia requires modification to consider the droplet inertia. Although other criteria have been proposed (e.g., [23]–[26]), it has been noted that

Ishii and Mishima's [21] criterion remains the most complete and tested criterion against a large number of experimental data [17], [27].

4 Experimental description

4.1 Description of facility

The two-phase serpent flow loop in the Oil and Gas Engineering Laboratory of Cranfield University (see Figure 2) is a specially built test facility used in the study of flow behaviour around upward and downward U-bends. It is divided into three main parts: the fluid supply (air and water) and metering area, the test area, and the separation section. The rig receives measured rates of water and air from the flow metering area to the test rig and finally into the ventilation tank, where the air and water are separated. The water is returned to the storage tank while the air is vented.

The test area consists of a flow loop, which is a diameter pipeline approximately 20-m long with a 4-inch (101.6-mm) internal diameter. It includes four ABS plastic vertical upward flowing and downward flowing sections connected by three Perspex 180-degree bends. The two middle 6-m vertical pipes are fitted with various instruments that collect all data. The right arm of the U is the downward flowing section, which is the area of interest of this study where all data were collected. The maximum discharge pressure of the compressors at 8 bar fixes the pressure rating of the facility, although typical test pressures are in the vicinity of 1.2 to 2 bar.

4.2 Instrumentation and experimental uncertainties

As shown in Figure 2c, a 32×32 WMS is used for air-water cross-sectional void distribution measurements at different locations along the pipe axis. Helmholtz–Zentrum Dresden–Rossendorf (HZDR), Germany, provided the sensor, accompanying electronics, and data-processing software. A number of studies [28]–[30] have validated the method of measuring the phase fraction distribution in air/water flows using similar WMS systems. Prasser et al. [28] used conductance 64×64 195 mm pipe, and void fraction measurements were taken from bubbly to churn turbulent flow near the transition region to annular flow. Da Silva et al. [29] used capacitance 24×24 on 67 mm pipe , Vieira et al. [31] 76 mm pipe 16×16 conductance, for annular flow.

In current the sensor assembly, two perpendicular sets of wire electrodes are stretched across the cross-sectional area of the flow. One set acts as a sender while the other acts as a receiver. The WMS electronics measures the local permittivity of the fluid in the gaps of each crossing point. This is accomplished by successively applying an excitation voltage to each one of the sender electrodes while keeping all other sender electrodes at ground potential and measuring the AC electrical current flow to all receiver electrodes in a synchronous manner. Based on these measurements, the cross-sectional fluid distribution across the pipe can be estimated. For the sensor used, the separation

between the sender and receiver planes of wires is 2.5 mm. The spacing between two parallel wires is 3.2 mm. The sampling rate is 1000 frames per second for the measurement. Further reading material can be found elsewhere [28], [32], [33] on the theory and principles of the WMS operation.

Conductance probes mounted on a probe spool measure the film thickness at a rate of 100 Hz. The spool consists of four sensors spaced 90˚ from each other to measure the circumferential distribution of the liquid film thickness at the axial location of the pipe where the spool is installed. Prior to two-phase flow experiments, the film thickness sensors were calibrated offline using acrylic blocks of different diameters, which were concentrically inserted into the probe spool to produce a liquid layer of known thickness. Temperature correction was applied for a range of 10–26℃, which covers the range of the experimental fluid temperatures. Tests on the repeatability of these liquid film sensors indicate an uncertainty margin of ±3.3%. [34]–[36] provide detailed descriptions, the design, and calibration, of the film thickness probes.

The mean film velocity was measured using an electrolyte injection method. This method is based on injecting sodium chloride electrolyte into the liquid film to cause a surge in its conductivity. A cross-correlation algorithm in MATLAB determines the transit time (or time delay) of a conductivity surge between two identical sensors 100 mm apart in the integrated probe spool. The film velocity (u_{lf}) is then calculated by dividing the distance between two sensors by the signal time delay. Though this method produces uncertainties of up to 20% for thin films at high gas flow rates [36], [37], most errors were around ±8% in the film velocity measurements. Here we define thin films as those satisfying t/D < 0.01 [38], [39]. Uncertainties in the liquid film mean velocity measurements can be introduced by following ways: (1) velocity distribution in the liquid film. Since the sensor electrode is flush mounted to the pipe, only conductivity values of the liquid in direct contact are registered; there is a discrepancy between the measured film velocity and the mean velocity, since the velocity profile in liquid film is not uniform. (2) The transit time measurement uncertainty which is limited by the sampling frequency of conductivity from the film velocity sensors. In this work, a frequency of 1000 Hz was employed meaning a 1 ms acquisition interval. For a typical transit time of 40 ms, this gives at least ±2.5% error in time delay determination by cross-correlation. (3) The design of the sensor electrodes with respect to their dimensions, such that partial contact is initially obtained with the electrolyte rather than almost instantaneous full contact if the electrode dimensions were of otherwise infinitesimal size. As the insulator part in the sensor is 1.0 mm wide, thus the uncertainty caused by this should be less than 1.0% for 1 sensor, and overall 2.0% for 2 sensors. (4) The velocity of electrolyte mixing/diffusion, which is mainly related to the injection rate and diffusivity of the electrolyte. It is estimated that the aforementioned sources of uncertainty could collectively give as much as ±8% error in the film velocity measurements, close to that reported by Al-Yarubi [37] and

Al-Yarubi and Lucas [40] in which similar method of film velocity determination in vertical air–water tests was used (See also [36])

A mass balance on the liquid flowing in the pipe section (Figure) provides a method of checking/validating the experimentally obtained film velocities. It is as follows:

$$\begin{pmatrix} Mass\ flow\ rate \\ of\ liquid\ into\ test \\ section \end{pmatrix} = \begin{pmatrix} mass\ flow\ rate \\ of\ liquid\ flowing \\ as\ \ film \end{pmatrix} + \begin{pmatrix} mass\ flow\ rate \\ of\ liquid\ flowing\ as \\ entrained\ droplets \end{pmatrix} \quad (7)$$

i.e.

$$\dot{m}_l = \dot{m}_{lf} + \dot{m}_E = \dot{m}_{lf} + e \cdot \dot{m}_l \quad (8)$$

where $\dot{m}_E$, $\dot{m}_l$, and $\dot{m}_{lf}$ are the entrained droplet mass flow rate, total liquid flow rate, and liquid film flow rate in kg/s, respectively. This gives:

$$\dot{m}_{lf} = \dot{m}_l(1 - e) \quad (9)$$

where e is the entrained droplet fraction. Given that the liquid film and pipe cross-sectional areas are geometrical parameters based on the schematic shown in Figure assuming fully developed flow where the film is cross-sectionally axis-symmetric. Substituting $\dot{m}_{lf} = \rho_l u_{lf} A_{lf} = \rho_l u_{lf} \pi t(D - t)$ and $\dot{m}_l = \rho_l u_{sl} A_{pipe} = \rho_l u_{sl} \frac{\pi D^2}{4}$ into Eq. (9) and simplifying, results in:

$$u_{lf} = \frac{u_{sl} D^2 (1-e)}{4t(D-t)} \quad (10)$$

where, u_{lf}, u_{sl}, and D are the entrained liquid fraction, measured film thickness, measured film velocity, liquid superficial velocity, and pipe internal diameter. Figure 4 shows a comparison of the experimental and mass balance derived film velocities. The error in the experimental film velocities are around the ±8% uncertainty whose sources were earlier discussed in the previous paragraph. The calculated film velocities are also not without errors. This is because input of experimental measurements (droplet fraction estimated using the WMS, and film thickness probes) is required. As discussed earlier, film thicknesses measured using the conductance probes produce an error margin of ±3% full-scale. The capacitance WMS used here was shown (see ref [41]) to produce uncertainties in the region of ±10%, but up to 20% errors are possible due to difficulty in detecting the gas liquid interface, nevertheless it is the best estimate available here for liquid velocity comparison purposes. As seen in Figure 4, these combine to produce large relative errors of up to 25% at some conditions and could be due high phase slip, which may not be properly captured in Eq. (10). At most conditions the values suggest the measured film velocities are not far from the calculated. The measured velocities were used to calculate the droplet fraction by carrying out a mass balance on the liquid phase and simplifying. This gives:

$$e = \frac{\dot{m}_E}{\dot{m}_l} = \frac{\dot{m}_l - \dot{m}_{lf}}{\dot{m}_l} = 1 - \frac{4u_{lf}t}{u_{sl}D} \quad (11)$$

This method was recently used by Al-Yarubi [37] and Van der Meulen [30]. More tabulated and graphical results obtained using Eq. (11) for different flow conditions have been published elsewhere [34], [36].

For uncertainty analysis, quantities with the most dominant contribution to the error in calculated entrained droplet fraction are the measured film thickness and film velocity. Assuming these are independent of each other, from Eq. (11), the error propagation can be expressed as follows:

$$\frac{E(e)}{e} = \sqrt{\left[\frac{E(t)}{t}\right]^2 + \left[\frac{E(u_{lf})}{u_{lf}}\right]^2} \quad (12)$$

where E is the error in the quantity enclosed in bracket and as stated earlier, the maximum random errors $E(t)$ and $E(u_{lf})$ are given as ±3.33% for the film thickness and ±8.00% for the film velocity respectively. These uncertainties for entrained droplet fraction determination for upflow have been plotted as the error bars given in Figure 5. Again, the maximum uncertainties of more than 16% are found at the high gas, high liquid flow conditions, but most lie between ±10% and ±12%.

Other methods exist for estimating the entrained droplet fraction such as film removal technique (see [42], [43]), and droplet sampling technique using isokinetic probes (see [11], [44], [45]). These have been widely used in the past and are not without their uncertainties which Cioncolini & Thome [9] pointed out mostly have to do with re-deposition of droplets during extraction and perturb the flow, for the former method. For the latter method where droplet concentration is measured and used to estimate the droplet fraction, uncertainties are introduced due to difficulty in distinguishing the interface between the wavy film and the gas core. This can lead to liquid from the film sampled and hence overestimating the droplet fraction.

5 Results and discussion

5.1 Flow regime identification, droplet size, and flow regime maps

Flow regime maps were produced using visual observation during tests and by studying high-speed videos and images of the flow, as well as studying the probability distribution functions (PDFs) of the WMS void fraction. For plots of the latter, the reader is referred to our earlier article [41]. Visual observations were made via transparent Perspex sections at the top, middle, and bottom sections of the test rig. Reconstructed videos from WMS sensor visualization were used to corroborate the visually obtained flow regimes and ultimately screen other flow regimes from the annular flow used for the analyses. The reconstructions were obtained by stacking acquired WMS cross-sectional images using specially designed software. These were used alongside visual observations for flow

regime identification, particularly to distinguish annular flow from other flow regimes such as churn and ensure the absence of pulsating flows.

Time-averaged cross-sectional void fraction data were used to produce the reconstructed images shown in Figure 6a and b. The figures show flow visualized at $u_{sl} = 0.30, \text{and } 1.0$ m/s respectively. In both figures, the liquid cross-sectional profiles are asymmetrical at the bottom positions (L/D = 5) and are more so at high gas velocities where the large gas momentum adds to the bend effect in causing massive flow maldistribution. However, on getting to the middle of the pipe (L/D = 30), the maldistribution is lessened more so at higher liquid flow in Figure 6b than at the lower liquid flow rate in figure (a). Nevertheless, complete axis-symmetry is achieved at the top positions of the pipe where L/D = 47 and the flow may be said to be highly developed. This observation is corroborated with profiles of the cross-sectional film thickness measurements given in Figure 7. For the middle and top axial positions, the profiles of the film thicknesses are similar and nearly uniform along the circumference. At the bottom position, however, the film thicknesses are generally thicker and not axis-symmetrical. A thicker water film always occurs at the pipe quadrant in the outermost part of the pipe circumference and bends. The near symmetry of the film at the middle and at the top position to a greater extent demonstrates the rapid decay of the centrifugal force acting around the bend as the flow progresses axially and this effect is almost non-existent on getting to L/D = 47. However, there is a lesser level asymmetry for the higher gas and liquid velocities as the mixture momentum gradually dominates the bend's centrifugal force. Indeed, as predicted by the criteria of Kataoka and Ishii [46], flow equilibrium is achieved at the following condition:

$$\frac{L}{D} = 440 \frac{We_g'^{0.25}}{Re_l^{0.5}} \tag{13}$$

where $We_g' = \frac{\rho_g u_{sg}^2 D}{\sigma}\left(\frac{\rho_l - \rho_g}{\rho_g}\right)^{1/3}$ is a densimetric Weber number. However, for our experimental conditions, this equation gave a maximum of L/D = 44 at the lowest tested superficial liquid velocity of 0.1 m/s. Higher superficial liquid velocities gave lower L/D values which were as low as 10, predicted by Eq. (13). Therefore, L/D = 47 used in the experiments provides sufficient development length for the flow to reach equilibrium and the data collected for the analyses in this paper were collected at this axial location. The other large diameter pipe study for entrained droplet fraction in annular flow found in the literature [47] had their entrained droplets measured at L/D = 40. For the present study, we believe that the upward flow section, where our measurements were taken, inherited the momentum of the previous section, which is downward flowing. The momentum is transferred upon negotiating the U-bend. This is different from other works where the flow starts only from bottom to top, and hence require up to L/D=100 for well-developed flow. However, for this study, good flow development was already achieved upon reaching L/D = 30.

To appreciate the depiction of droplets by the reconstructed WMS images in Figure 6, knowledge of typical droplet sizes is required. Since the spacing between neighbouring wires in the WMS is 3.2 mm, interaction with droplets is likely to be maximised in the presence of larger droplets. Conversely, more finely dispersed droplets are likely to pass through without interacting with the wires, which are 0.1 mm thick. Nevertheless, the sensor wires always sense the equivalent capacitance of air/droplets despite droplet size. Drop size was not measured, but five reported correlations were used to estimate the mean entrained droplet size based on the flow conditions, pipe diameter, and fluid properties. This mean size, known as the Sauter mean diameter d_{32}, is usually measured using optical methods. Berna et al. [48] noted that Sauter mean diameters are typically correlated using power law equations with the general form,

$$\frac{d_{32}}{D} = K \cdot Re_g^a Re_l^b We_g^c \left(\frac{\rho_g}{\rho_l}\right)^d \left(\frac{\mu_g}{\mu_l}\right)^e \tag{14}$$

where D is the pipe diameter, ρ and μ are the fluid densities and dynamic viscosities, respectively, while K and a–e are regression constants. The Reynolds and Weber numbers are expressed in terms of the superficial fluid velocities and pipe diameter. The regression constants determined in other studies are given in Table 1 [49]–[51]. Instead of using a liquid Reynolds number, Azzopardi et al. [52] added a second term to Eq. (14) to account for the effect of liquid flow rate on drop size:

$$\frac{d_{32}}{D} = 1.91 Re_g^{0.1} We_g^{-0.6} \left(\frac{\rho_g}{\rho_l}\right)^{0.6} + 0.4 \frac{\dot{e}}{\rho_l u_{sg}} \tag{15}$$

where $\dot{e}$ is the entrainment mass flux (in kg/m^{2}s). Al-Sarkhi and Hanratty [53] constructed a model using drop size measurements in a 13-mm ID pipe. A simplified version of their correlation that does not depend on the entrainment mass flux is as follows:

$$\left(\frac{d_{32}\rho_g u_{sg}^2}{\sigma}\right)^{0.55} \left(\frac{d_{32}}{D}\right)^{0.36} = 0.154 \tag{16}$$

Figure 8 presents the mean droplet sizes estimated by Eqs. (14)–(16) for the current experimental setup and are presented against the superficial gas velocity. The mean droplet diameter varies inversely with u_{sg}, and the correlations generally predict most droplets to be smaller than the 3.2-mm mesh spacing of the WMS. This is especially so at higher gas flow where the droplets are more or less atomised, thus raising their likelihood of passing the wires without interaction. We can hence conclude that the WMS has negligible disturbance effect on droplet flow.

Figure 9a shows the flow regime map for upward flow, where annular flow occurs in the range 9–30 m/s for liquid superficial velocities of 0.1–1.0 m/s. Non-annular flow regimes marked as "other" in the figure are either bubbly or churn flow and are not within the scope this study. The regimes were identified with the help of videos made from WMS reconstructed images. Specially designed software was used to stack the images acquired at 1000 fps and these can be played back at slower speeds than

real-time. Typical snapshots of such videos were taken and these are shown above Figure 9a, and they refer to flows at u_{sl} = 9.7, and 14.1 m/s at the liquid condition of u_{sl} = 0.2 m/s. It can be seen that for the former condition, the gas core is not in continuum. Large liquid chunks can be seen to rise from base film, some completely entrained into the gas core. Such a flow cannot be said to be annular since some up and down oscillatory movement exist. The regime was ultimately categorised as "churn" flow and screened out from those used for analysis and comparison. Such flow regime discrimination is difficult to achieve with the naked eye. Conversely, the snapshot on the top right-hand corner of Figure 9a can be classified as annular. It shows a distinct gas–liquid interface and a clear gas continuum exists. Droplets are visibly entrained in the core. Figure 9b shows the test velocities of the superficial gas and liquid for downward flow. The experimental conditions designated as "annular" include both falling film and annular flow regimes, while those marked as "others" indicate bubbly or churn flow regimes. Unlike the upward flow, the region where annular flow occurs is wider ($u_{sg} = 1.1 - 29\ m/s$) due to gravity and inertial forces acting in the same direction. These behaviours have been described in more detail in earlier studies using the same experimental setup [34], [41].

5.2 Other data from published sources

Two of the studies used to assess the current prediction methods were conducted with large-diameter tubes, while 27 were used smaller diameter pipes. These are presented chronologically in Table 2. Azzopardi et al. [47] conducted an adiabatic large-pipe study using air and water in a 125-mm vertical column. They indirectly measured the fraction of entrained droplets using the film withdrawal technique first devised by Whalley et al. [58]. They noted that disturbance waves in their experiments lacked many of the features observed in small-diameter pipes. For example, these disturbance waves were circumferentially localised rather than ring-shaped over the entire circumference, as well as bow-shaped rather than perpendicular to the flow direction. This lends more credence to assertions that two-phase flow behaves differently in large pipes i.e. those with diameter greater than 100 mm. Van der Meulen [30] from the University of Nottingham performed the other large-pipe experiments with a 127-mm-diameter pipe at around 2 bar. The entrained droplet fraction was measured using the same method as in the present study, where the film flow rate is estimated by measuring its velocity. While their flow conditions traversed both the churn-turbulent and annular regimes, care was taken in the present work to select data in only the annular flow region, and 31 data points were obtained.

The remaining 27 small-diameter pipe studies examined both adiabatic and diabatic flows. The adiabatic flows mainly consist of air/water studies with the exception of Jepson et al. [59], who used helium and water, as well as Fore et al. [60] and Alamu [61], who used air and glycerine mixtures. For the diabatic flow studies, experiments involving condensation dominate, and we present them as steam and water flows. These investigations provided a total of 290 data points and use pressures of 30–90 bar [62], [63], [64]. For such experiments, it is more convenient to work in terms of the total

mass flux and the vapour quality *x*. Mass balances are then used to calculate the superficial liquid and gas (or vapour) velocities as follows:

$$u_{sg} = Gx/\rho_g \; and \; u_{sl} = G(1-x)/\rho_l \quad (17)$$

where G is the total mass flux and

$$x = \rho_g u_{sg}/(\rho_g u_{sg} + \rho_l u_{sl}) \quad (18)$$

When vapour or gas density was not provided, we looked up the values in steam tables at the specified test pressure for our calculations.

The remaining diabatic studies involved refrigerants in channels with diameters of 10–14 mm. For the experiments of [65], R12 was the working fluid in a 14-mm vertical pipe, and film withdrawal was the indirect method used to measure the entrained mass flow rate. Ueda and Kim [66], Lopez de Bertodano [67] and Sawant et al. [27] used the refrigerant Freon R113 as the fluid using flow loops fitted with 10-mm test sections and the film removal method to measure e. These four studies provided 119 data points for our analyses.

Figure 10a displays all 1,391 data points. These were plotted on Hewitt and Roberts' [68] flow regime map and show that the flow conditions fall in the annular and wispy-annular flow regions. Only eight data points fall along the boundary of churn and annular flow. Since flow regime transitions are not sharp and occur over a range, these points are considered as annular flow data. In Figure 10b are the conditions plotted on the Taitel et al. [69] flow regime map. Taitel and co-workers developed this flow regime map using various transition criteria, which include analytical relationships for the force balance between gravity and drag forces acting at the onset of annular flow. They validated their flow transition criteria with data obtained from a 50-mm diameter pipe. Superimposed on the flow regime map are the observations made by various other authors in 152–203 mm pipes [28], [70], [71]. In all the observed flow regimes by these authors, transition to annular agreed with that predicted by Taitel et al.'s [69] flow regime map. However, the observations in the larger-diameter pipes produced wider regions for the occurrence of bubbly flow as more spherical cap bubbles are produced than in smaller pipes. This is because, slug flow is absent from the large-pipes due to the Rayliegh-Taylor instability preventing the formation of Taylor bubbles once D > 100 mm.

5.3 Comparison of data with literature correlations

Many correlations for the entrained droplet fraction have been developed in the last half century. Direct correlation using the entrained liquid fraction is most common, but some authors prefer correlations using the entrained droplet flow rate. The latter can be converted easily to the former by simply dividing by the total liquid flow introduced in the pipe. Table 3 summarises the features of the fifteen correlations for the entrained droplet fraction.

With the exception of [6], dimensionless numbers are used to correlate the data, although the exponents $\beta_0 - \beta_9$ given in Table 4 make Oliemans et al.'s [6] correlation dimensionless overall. Its implementation is iterative, but comparisons with the data given in Figure 11 show that it is one of the most successful among the surveyed correlations.

The gas Weber number is a popular non-dimensional number used by many of the investigators to produce their correlations [4], [9], [21], [50], [56]. This is because it is a ratio of the gas inertial forces to surface tension forces within the liquid, which are dominant in determining the amount of droplets entrained from the liquid film. Cioncolini and Thome [9] note that the Weber number is especially used in the investigation of multiphase flows characterised by an interface separating two fluids, with particular importance in spray theory. Therefore, the common usage is not surprising since the number is consistent with flow phenomena containing liquid droplets in a gas such as annular flow. The phase Reynolds and Froude numbers are also widely used when employing the velocity and density ratios. Regardless of the combination of dimensionless numbers used, the range of conditions from which the data were obtained ultimately determines the success of the correlation since pure theoretical models that describe e have not yet been derived.

Table 3 also shows that the various correlations were developed using a wide variety of system pressures, fluid combinations, and pipe diameters. These all affect the success of a correlation when used for a system where these conditions may be similar or differ to varying degrees. One key similarity between all the correlations is that their source data were all obtained from pipes of small diameter (less than 100 mm). As a result, the plots in Figure 11 comparing the predictions of four of the best performing correlations with the current database (given in Table 2) show that large deviations can result in many cases.

Statistical parameters were used to quantify the deviations between the experimental and predicted points by each correlation. These are the mean absolute deviation (MAD) percentage and the mean square error (MSE):

$$\text{MAD} = \frac{1}{n}\sum_i^n \left|\frac{e_{i,exp} - e_{i,pred}}{e_{i,exp}}\right| \times 100 \tag{19}$$

$$\text{MSE} = \frac{1}{n}\sum_i^n \left(e_{i,exp} - e_{i,pred}\right)^2 \tag{20}$$

where the subscripts *exp* and *pred* indicate "experimental" and "predicted", respectively, while n is the total number of points compared. The four sample correlations in Figure 11 produced similar MSE values of around 0.1, with the best MSE resulting from the correlation of Ishii and Mishima [21]. Their correlation also gave the best MAD value of 56.4%, while that of [4] gave the lowest value. However, many of [21] predictions clustered near $e = 1$, indicating a bias towards large entrained

fractions. Along with the other correlations, up to 55% of the predicted points lie outside the ±50% error band.

The discrepancies do not seem to cut across diabatic or adiabatic flows, which explains why no authors have produced correlations to cater exclusively to either group of flows. In addition, while viscous liquids tend to produce more entrained droplets because of lower surface tension, there was no segregation of the predictions based on this in our comparative analysis. Significant factors that influence the deviation between correlations and given sets of data include pipe diameter, pipe geometry (e.g. round or rectangular cross-section), range of experimental conditions (e.g. pressure and superficial velocities), and gas/liquid combination, and fluid physical properties (especially liquid viscosity, and surface tension). Pipe diameter has been identified as a leading factor that determines multiphase flow behaviour, but since the correlations were developed using data from numerous sources, varying degrees of random experimental errors could affect their predictive capabilities. For example Oliemans et al. [6] developed their correlation using a 727 data points from 18 different sources where different methods were used to measure the entrained droplet fraction and potentially varying degrees of error. Data from air–ethanol, air–hydrocarbon, and steam–water combinations were also part of their database, in addition to an air–water fluid combination. This disparity in types of fluids used is similar to that collected for the present study where entrained droplet data for air – water, air–glycerine, helium– water, steam–water, and refrigerants R112, and R113 were obtained. The pipe diameters for the database Oliemans and co-workers used range from 9.5 to 31.8 mm – all small diameter pipes. This means that the most distinctive feature between their database for their correlation and our data is the pipe scale since ours contains data from pipes of up to 127-mm internal diameter. A look at the plot of their correlation against our databank (Figure 10b) reveals consistent under-predictions of the large diameter pipe data by the correlation. Due to pipe diameter ranges being the main difference with our data, we suspect that the deviations are largely because of this. A similar reason could be adduced for the deviations produced by Ishii and Mishima's [21] as well as Cioncolini and Thome's [72] correlations' given the comparable diversity of their data sources. Furthermore, the Cioncolini – Thome correlation gives sole dependence of the entrained fraction on the core Weber number. As droplet entrainment in annular two-phase flow is a complex phenomenon involving surface tension, inertial, and body forces acting on either side of the gas–liquid interface, hardly will one dimensionless group adequately the effect of all the forces. Nevertheless, it produced creditable predictions of the current databank with a mean absolute deviation (MAD) of ±60% second only to the Ishii–Mishima correlation (MAD = ±56%) among the four correlations tested. The Paleev and Filippovich [4] database is less disparate in comparison with the previously mentioned as it contains only data of air–water from six different studies; and could be the main source of it deviations. A majority of data are beyond the 50% error band and are mainly under-predictions. This could mean that larger entrained droplet fractions are obtained in pipes of larger diameter, since such

pipes have more core space for re-deposition to become less likely than smaller pipes. This is an important consideration for the design of downstream separation equipment such as scrubbers and hydro-cyclones. Underestimating the amount of entrained liquid droplets can affect the quality of separations. Overall it appears new correlations must be developed with databanks that are updated with measurements from large-diameter pipes.

Previously, Aliyu et al. [73] produced a correlation for the entrained droplet fraction using the large-diameter data in the present database given in Table 2. Specifically, data from the works of Van der Meulen [30] and Azzopardi et al. [47] were used in addition to those obtained using the experimental flow loop of this study. All the test fluids for the three studies were air and water at system pressures of 2 bar and below. Therefore, the correlation does not give adequate predictions for higher system pressures of steam/water or refrigerant flows in small-diameter pipes.

In finding a relation for the entrained droplet fraction that fits the entire database, the Weber number We, gas Reynolds number Re_g, and liquid Reynolds number Re_l were selected as correlating dimensionless groups. Both Reynolds numbers are based on superficial gas velocities and the whole pipe diameter as the significant length scale. The choice of the Reynolds numbers is expected as is the case in many fluid mechanics problems, and this is based on the ability of the Reynolds to capture fluid inertia changes. In the database, these are all in the range of $5 \times 10^3 - 10^4$ in the turbulent region where flow momentum far dominates viscous forces. The choice of the Weber number is because it is especially used in the investigation of multiphase flows characterised by an interface separating two fluids. As explained by Cioncolini and Thome [10], it is a particularly controlling dimensionless number generally used in spray theory and is used in studying liquid atomisation and in the study of surface tension waves on shear-driven liquid films. In annular two-phase flow, the core flow can be considered as a spray interacting with the liquid film, which is shear driven by the core flow and characterised by surface tension waves appearing at its surface. The crests of such waves are atomised by flowing gas in the core hence producing entrainment. While they used weber number based only of the properties of the flowing gas in obtaining their correlation, they conceded that the use of a Weber number defined using a velocity difference is more accurate, but the improvement in accuracy is not appreciable. Nevertheless, the Weber number was influential enough to be used alone in correlating their entire database, which contains disparate fluid combinations, properties and pipe diameter. Therefore, the selection of the Weber number here as a correlating group is consistent with the phenomena of annular flow. We define the Weber here selected as follows:

$$We = \frac{\rho_g u_{sg}^2 D}{\sigma}\left(\frac{\Delta\rho}{\rho_g}\right)^{1/4} \tag{21}$$

where $\Delta\rho = \rho_l - \rho_g$. This Weber number is densimetric and it was used by Sawant et al. [74] to correlate their droplet fraction data, a modified form from the original one where the density ratio was raised to the index $^1/_3$. Both were tested with the current databank and ¼ seemed to correlate better. Therefore, we can write the entrained droplet fraction as a function of the dimensionless groups as follows:

$$\frac{e}{(1-e)} = A \cdot We^b \, {Re_g}^c {Re_l}^d \tag{22}$$

where *A*, *b*, *c*, and *d* are constants to be determined by fitting the collected experimental data to Eq. (22). The use of the entrained droplet ratio $e/(1-e)$ rather than just e is based on a simple argument in that droplet fraction has been shown to be directly dependent on the liquid film Reynolds number (see [6] for example). i.e.

$$e \propto Re_{lf} \tag{23}$$

But since by definition, the film Reynolds number $Re_{lf} = Re_l(1-e)$, substituting in Eq. (23) gives the dependence as follows:

$$e \propto Re_l(1-e) \tag{24}$$

hence,

$$\frac{e}{(1-e)} \propto Re_l \tag{25}$$

This is consistent with the selection of the liquid Reynolds as a correlating dimensionless number in Eq. (22). Moreover, this avoids producing values of e greater than unity, which if were to be the case, is indeed physically meaningless. One obvious quantity that could be added to the right hand side of Eq. (22) is the dimensionless film thickness t/D. While this was measured in the current experiments and a few others in the database, it is largely unavailable for the large majority of studies. An approach that can be employed to obtain this is by the use of correlations. However, with a large database in which there is great variety in flow conditions, fluid property, and pipe size, the question arises: which correlation is suitable? There are very many film thickness correlations in the literature, which were derived for specific fluid combinations and pipe sizes, and deciding on one for use here will introduce a large amount of error. In their analysis, Bertodano et al. [67] noted that Wallis' [75] work on sand grain roughness in which it was found out that $t \approx 4\delta$ (the variable δ is the height of disturbance wave). This reasoning was used to avoid the problem of lack of experimental data because of difficulty in measuring such a variable. While we note the importance of t/D as a group that affects entrainment. Based on this, t/D was not included as a correlating group in Eq. (22), but we note the mere presence of a film is critical for entrainment to occur. By keeping this term, the non-entrained flow conditions can be well explained and future correlations can be improved with

increased availability of experimental t/D data. For the current work, it is deemed that using t/D from correlations introduces too much uncertainty that is difficult to quantify.

To obtain the constants *A*–*d* in Eq. (22), we used the entire database. The database comprises 1,391 data points from 29 studies, including the present experiments. These data include those from large and small-diameter pipes; adiabatic flows for air–water, air–glycerine, and helium–water fluid combinations; and evaporating and condensing flows involving steam–water fluid mixtures as well as the refrigerants R12 and R113. The method of nonlinear least squares is a powerful technique that can be easily implemented in a spreadsheet package (such as Microsoft Excel®) for the determination of the proposed correlation's constants. To do this, we rewrite Eq. (22) as follows:

$$r_i = \left[\frac{e}{(1-e)}\right]_{exp,i} - \left[A \cdot We^b \, {Re_g}^c {Re_l}^d\right]_{pred,i} \tag{26}$$

where *r* is the residual being the difference between each experimental point (*exp*) and corresponding predicted point (*pred*) *i*. A value of $r_i = 0$ is the ideal target, though difficult to achieve due to random errors in experimental measurements. There is no closed-form solution for Eq. (26) and an infinite number of solutions exist. Hence, the best values for the coefficient *A* and indices *b*–*d* are those that gives the minimum value of the sum of squares of the residuals *S* across the entire experimental database, and this is found by solving the nonlinear least squares minimisation problem:

$$min\, S = \sum_{i=1}^{N} {r_i}^2 = \sum_{i=1}^{N} \left\{ \left[\frac{e}{(1-e)}\right]_{exp,i} - \left[A \cdot We^b \, {Re_g}^c {Re_l}^d\right]_{pred,i} \right\}^2 \tag{27}$$

where *N* is the number of data points in the databank. Eq. (27) is solved iteratively using the Gauss–Newton deterministic algorithm embedded in the Solver® add-in in Microsoft Excel. Initial values for *A*–*d* were given and these were chosen to be as physically realistic as possible in order to help the algorithm converge easily and to a solution with realistic coefficients. For example, since $e/(1-e) \propto Re_l$, the index *d* can only take positive values, and a positive number initial guess for *d* is made. After implementing the algorithm, the following relationships were obtained:

$$\frac{e}{(1-e)} = \begin{cases} 2.00 \times 10^{-3} \cdot We^{0.5} \, {Re_g}^{0.0001} {Re_l}^{0.29} & \text{for } u_{sg} > 40\ m/s \\ 1.24 \times 10^{-3} \cdot We^{0.15} \, {Re_g}^{0.20} {Re_l}^{0.23} & \text{for } u_{sg} \le 40\ m/s \end{cases} \tag{28}$$

(29)

In Eq.(28), the index of Re_g is a very small number→0 (i.e. 0.0001), signifying that the correlation between the entrained droplet fraction and the gas Reynolds number is weak at high gas velocities. This means that at some point beyond $u_{sg} = 40\ m/s$, increasing gas flow does not result in a marked increase in the entrained droplet fraction in the gas core. This observation is supported by plots of *e* vs. u_{sg} for different superficial liquid velocities, as shown in Figure 12 for the studies by Wicks and Dukler [20], Owen [73] and Sawant et al. [74], whose experimental conditions had data

points exceeding $u_{sg} = 40\ m/s$. Therefore, We_g may be considered sufficient for representing the dependency on gas flow on droplet entrainment in this region. The gas Reynolds number can be omitted altogether from Eq. (28), and this gives:

$$\frac{e}{(1-e)} = 2.00 \times 10^{-3} \cdot We^{0.5}\ {Re_l}^{0.29} \text{ for } u_{sg} > 40\ m/s \tag{28a}$$

If Eqs. (28a) and (29) are rewritten so that an explicit relationship is established for e, they take the following form:

$$e = \begin{cases} \frac{1.00\times10^{-2}\cdot We^{0.33}\ {Re_l}^{0.27}}{1+\left[1.00\times10^{-2}\cdot We^{0.33}\ {Re_l}^{0.27}\right]} & \text{for } u_{sg} > 40\ m/s \\ \frac{1.25\times10^{-3}\cdot We^{0.15}\ {Re_g}^{0.20} {Re_l}^{0.23}}{1+\left[1.25\times10^{-3}\cdot We^{0.15}\ {Re_g}^{0.20} {Re_l}^{0.23}\right]} & \text{for } u_{sg} \leq 40\ m/s \end{cases} \tag{30}$$

(31)

Figure 13 is a plot of Eqs. (30) and (31) against the experimental entrained droplet fractions. Over the entire database, these equations correlate the entrained droplet fractions quite well. In comparison to the MAD and MSE obtained for the previous correlations shown in Figure 11, the 39.6% and 0.031 produced by the new correlations are appreciable improvements. Also, 74% of the new predictions occur within the ±50% error region, in contrast to the 44, 56, 61, and 58% given by the correlations by [4], [6], [9], [21] respectively.

Selected simulations showing the predictions of our derived correlation for various studies are included in Figure 14. As seen in Figure 14a, both the trend and accuracy of the e predictions are satisfactory at high gas velocities when compared with the air/water experiments of Owen [73] and Sawant et al. [74] at superficial liquid velocities of 0.035 and 0.05 m/s, respectively. Only the smallest entrained droplet fraction for data by [57] at around $u_{sg} = 30\ m/s$ produced a large deviation from the correlation. These data could be considered outliers since most of the data for the high gas velocities were well predicted. Similarly, the correlations produced good predictions for the Freon R113 refrigerant data by Sawant et al. [27] and Lopez de Bertodano et al. [63].

The dimensionless numbers here were chosen heuristically. Even in a situation where rigorous dimensional analysis is employed, the groups that emerge by no means signify that the entrained liquid fraction depends only on the groupings that finally emerge. As such, Weber, and Reynolds numbers used here are not the only parameters that affect the droplet fraction. Instead, it is quite likely that the significant scatter in the available databank is large enough to hide any fine details in the data. In fact, a near exhaustive dimensional analysis by Cioncolini and Thome [9] identified 19 different groups that could be correlated with the entrained droplet fraction. These include the Ohnesorge and Froude numbers as well as velocity, density, and viscosity ratios, but a correlation with all of them will be too cumbersome and may altogether be impractical. It can be shown that

many of the dimensionless numbers can be combined to give the Reynolds and Weber numbers or functions of them e.g. the Ohnesorge is the ratio: $\sqrt{We}/Re$. Even so, the addition of further groups may only result in a marginal increase in accuracy. However, within the limits of the present study, the three used here appear to show reasonable correlation with the entrained fraction, and significant scatter beyond ±50% still occurs. Possible use of improved experimental methods such as laser techniques for droplet identification may reduce the shortcomings of the methods used in the past and hence lessen scatter. Furthermore, derivation of analytical relationships based on underlying flow physics offers the best chance of obtaining much more reliable models for droplet entrainment as well as other multiphase flow parameters (e.g. liquid film thickness) that will be applicable to a wider range of conditions. These can then be plugged into existing numerical computational fluid dynamics (CFD) codes to improve prediction. Examples of such codes are those implemented [77]–[80] for the steady/unsteady 1-dimensional 3-field (or fluid) model in which phase fractions are obtained simultaneously along pipe sections.

6 Conclusions

The entrained droplet fraction was measured in a 101.6-mm large-diameter pipe flow rig using film velocity measurements in the annular flow regime. Together with published data on droplet entrainment in large-diameter pipes obtained by Van der Meulen [30] (127 mm) and Azzopardi et al. [47] (125 mm), other droplet fraction measurements carried out in smaller pipes were also acquired. These produced an experimental database of 1,391 data points, and comparisons were made with predictions of several published empirical correlations. Large deviations between these predictions and the experimental data were established, especially those obtained with larger pipes. Higher droplet fractions were obtained in larger pipes, perhaps because increased core space makes droplet re-deposition more unlikely. This is in line with observations by previous authors, such as Azzopardi et al. [47], who observed different disturbance wave characteristics in larger pipes. These disturbance waves have long been known as sources of droplets, which are sheared into the gas core.

To cater for the observed inadequacies of correlations (developed using experiments on pipes of 5–95-mm diameter), another correlation for the entrained liquid fraction was obtained using the available databank. However, more data must be collected for even larger pipes of 150-mm ID and above (which represent the sizes of typical industrial pipes), for higher gas velocities of 30–100 m/s, and for more viscous liquids, for which the current database is somewhat deficient.

7 Acknowledgement

A. M. Aliyu and Y. D. Baba would like to express sincere gratitude to the Petroleum Technology Development Fund, Abuja for the grants: PTDF/E/OSS/PHD/AMA/622/12 and PTDF/E/OSS/PHD/BYD/532/12, respectively. This work was also supported by the National

Research Foundation of Korea (NRF) grant funded by the Korean government (MSIP) through GCRC-SOP (No. 2011-0030013). We also acknowledge the funding provided by the BK21 Plus Program of the School of Mechanical Engineering, Pusan National University, Republic of Korea. Finally, for data processing, image reconstruction software, and technical support, we thank Prof. Hampel and his group at Helmholtz-Zentrum Dresden-Rossendorf, Germany, as well as Prof. Da Silva and his group at Universidade Tecnológica Federal do Paraná, Brazil.

8 References

[1] C. Berna, A. Escrivá, J. L. Muñoz-Cobo, and L. E. Herranz, "Review of droplet entrainment in annular flow: Interfacial waves and onset of entrainment," *Prog. Nucl. Energy*, vol. 74, pp. 14–43, 2014.

[2] G. F. Hewitt, "Co-Current and Counter-Current Two Phase Annular Flow," *9th Australasian Fluid Mechanics COnference*. pp. 19–28, 1986.

[3] G. F. Hewitt and N. Hall Taylor, *Annular Two-phase Flow*. Oxford: Pergamon Press, 1970.

[4] I. I. Paleev and B. S. Filippovich, "Phenomena of liquid transfer in two-phase dispersed annular flow," *Int. J. Heat Mass Transf.*, vol. 9, no. 10, pp. 1089–1093, Oct. 1966.

[5] G. B. Wallis, "Phenomena of liquid transfer in two-phase dispersed annular flow," *Int. J. Heat Mass Transf.*, vol. 11, no. 4, pp. 783–785, Apr. 1968.

[6] R. V. A. Oliemans, B. F. M. F. M. Pots, and N. Trompé, "Modelling of annular dispersed two-phase flow in vertical pipes," *Int. J. Multiph. Flow*, vol. 12, no. 5, pp. 711–732, Sep. 1986.

[7] G. F. Hewitt and A. H. Govan, "Phenomenological modelling of non-equilibrium flows with phase change," *Int. J. Heat Mass Transf.*, vol. 33, no. 2, pp. 229–242, Feb. 1990.

[8] L. Pan and T. J. Hanratty, "Correlation of entrainment for annular flow in vertical pipes," *Int. J. Multiph. Flow*, vol. 28, no. 3, pp. 363–384, 2002.

[9] A. Cioncolini and J. R. Thome, "Prediction of the entrained liquid fraction in vertical annular gas-liquid two-phase flow," *Int. J. Multiph. Flow*, vol. 36, no. 4, pp. 293–302, 2010.

[10] A. Cioncolini and J. R. Thome, "Entrained liquid fraction prediction in adiabatic and evaporating annular two-phase flow," *Nucl. Eng. Des.*, vol. 243, pp. 200–213, 2012.

[11] J. R. Barbosa, G. F. Hewitt, G. König, and S. M. Richardson, "Liquid entrainment, droplet concentration and pressure gradient at the onset of annular flow in a vertical pipe," *Int. J. Multiph. Flow*, vol. 28, no. 6, pp. 943–961, 2002.

[12] P. F. Pickering, G. F. Hewitt, M. J. Watson, and C. P. Hale, "The prediction of flows in

production risers - truth and myth?," in *IIR Conference*, 2001, pp. 1–16.

[13] J. P. Schlegel, S. Miwa, S. Chen, T. Hibiki, and M. Ishii, "Experimental study of two-phase flow structure in large diameter pipes," *Exp. Therm. Fluid Sci.*, vol. 41, no. 2012, pp. 12–22, Sep. 2012.

[14] L. Lao, L. Xing, and H. Yeung, "Behaviours of elongated bubbles in a large diameter riser," in *8th North American Conference on Multiphase Technology (Multiphase 8)*, 2012, no. 1998, pp. 381–392.

[15] F. H. Garner, S. R. M. Ellis, and J. A. Lacey, "The size distribution and entrainment of droplets," *Trans. Inst. Chem. Eng.*, vol. 32, pp. 222–235, 1954.

[16] D. M. Newitt, N. Dombrowski, and F. H. Knelman, "Liquid Entrainment: The Mechanism of Drop Formation from Gas or Vapour Bubbles," *Trans. Inst. Chem. Eng.*, vol. 32, no. 244, 1954.

[17] K. K. Kuo and F. B. Cheung, "Droplet Entrainment of Breakup by Shear Flow," pp. 1–56, 1995.

[18] R. Kaji and B. J. Azzopardi, "The effect of pipe diameter on the structure of gas / liquid flow in vertical pipes," *Int. J. Multiph. Flow*, vol. 36, no. 4, pp. 303–313, 2010.

[19] A. Frohn and N. Roth, *Dynamics of droplets*. Springer Science & Business Media, 2000.

[20] M. Wicks and A. E. Dukler, "Entrainment and pressure drop in concurrent gas-liquid flow: air-water in horizontal flow," *AIChE J.*, vol. 6, p. 463, 1960.

[21] M. Ishii and K. Mishima, "Droplet entrainment correlation in annular two-phase flow," *Int J Heat Mass Transf.*, vol. 32, no. 10, pp. 1835–1846, Oct. 1989.

[22] M. Ishii and M. A. Grolmes, "Inception criteria for droplet entrainment in two-phase concurrent film flow," *AIChE J.*, vol. 21, no. 2, pp. 308–318, Mar. 1975.

[23] G. B. Wallis, "The onset of droplet entrainment in annular gas-liquid flow," General Electric Co. General Engineering Lab., Schenectady, NY, 1962.

[24] S. S. Kutateladze, "Elements of the hydrodynamics of gas-liquid systems," *Fluid Mech. Res.*, vol. 1, no. 4, pp. 29–50, 1972.

[25] N. Zuber, "On the Atomization and Entrainment of Liquid Films in Shear Flow," *Gen. Electr. Co. Rep.*, vol. 62, 1962.

[26] R. T. Jensen, *Inception of liquid entrainment during emergency cooling of pressurized water reactors*. 1971.

[27] P. Sawant, M. Ishii, and M. Mori, "Prediction of amount of entrained droplets in vertical annular two-phase flow," *Int. J. Heat Fluid Flow*, vol. 30, no. 4, pp. 715–728, 2009.

[28] H.-M. Prasser *et al.*, "Evolution of the structure of a gas–liquid two-phase flow in a large vertical pipe," *Nucl. Eng. Des.*, vol. 237, no. 15–17, pp. 1848–1861, Sep. 2007.

[29] M. J. Da Silva, S. Thiele, L. Abdulkareem, B. J. Azzopardi, and U. Hampel, "High-resolution gas–oil two-phase flow visualization with a capacitance wire-mesh sensor," *Flow Meas. Instrum.*, vol. 21, no. 3, pp. 191–197, Sep. 2010.

[30] G. P. Van der Meulen, "Churn-Annular Gas-Liquid Flows in Large Diameter Vertical Pipes," PhD Thesis, University of Notingham, 2012.

[31] R. E. Vieira *et al.*, "Experimental characterization of vertical gas-liquid pipe flow for annular and liquid loading conditions using dual Wire-Mesh Sensor," *Exp. Therm. Fluid Sci.*, vol. 64, pp. 81–93, 2015.

[32] M. J. Da Silva, E. Schleicher, and U. Hampel, "Capacitance wire-mesh sensor for fast measurement of phase fraction distributions," *Meas. Sci. Technol. Meas. Sci. Technol*, vol. 18, no. 18, pp. 2245–2251, 2007.

[33] M. J. Da Silva, S. Thiele, L. Abdulkareem, B. J. Azzopardi, and U. Hampel, "High-resolution gas – oil two-phase flow visualization with a capacitance wire-mesh sensor," *Flow Meas. Instrum.*, vol. 21, no. 3, pp. 191–197, 2010.

[34] A. A. Almabrok, "Gas - Liquid two-phase flow in up and down vertical pipes," PhD Thesis, Cranfield University, 2014.

[35] A. M. Aliyu, "Vertical annular gas-liquid two-phase flow in large diameter pipes," Cranfield University, 2015.

[36] A. M. Aliyu, L. Lao, A. A. Almabrok, and H. Yeung, "Interfacial shear in adiabatic downward gas/liquid co-current annular flow in pipes," *Exp. Therm. Fluid Sci.*, vol. 72, pp. 75–87, 2016.

[37] Q. Al-Yarubi, "Phase flow measurements of annular flows," University of Huddersfield, 2010.

[38] A. S. Telles and A. E. Dukler, "Statistical Characteristics of Thin, Vertical, Wavy, Liquid Films," *Ind. Eng. Chem. Fundam.*, vol. 9, no. 3, pp. 412–421, Aug. 1970.

[39] J. C. Asali, T. J. Hanratty, and P. Andreussi, "Interfacial Drag and Film Height for Vertical Annular Flow," *Am. Inst. Chem. Eng.*, vol. 31, no. 6, pp. 895–902, 1985.

[40] G. Al-Yarubi, Q. Lucas, "Measurement of the Film Thickness, Film Velocity, and Entrainment

Fraction in a Liquid-Air Annular Flow using a Conductance Flowmeter," *Comput. Eng. Annu. Res. Conf.*, pp. 63–68, 2008.

[41] A. A. Almabrok, A. M. Aliyu, L. Lao, and H. Yeung, "Gas/liquid flow behaviours in a downward section of large diameter vertical serpentine pipes," *Int. J. Multiph. Flow*, vol. 78, pp. 25–43, 2016.

[42] K. Sekoguchi, O. Tanaka, and T. Ueno, "On the Determination Method of Entrained Droplet Flow Rate in the Disturbance Wave Region of Annular Flow," *Bull. JSME*, vol. 28, no. 240, pp. 1105–1112, 1985.

[43] B. J. Azzopardi and S. Zaidi, "Determination of Entrained Fraction in Vertical Annular Gas / Liquid Flow," *Asme*, vol. 122, no. March 2000, pp. 146–150, 2000.

[44] L. E. Gill, G. F. Hewitt, and P. M. C. Lacey, "Sampling probe studies of the gas core in annular two-phase flow—II," *Chem. Eng. Sci.*, vol. 19, no. 9, pp. 665–682, Sep. 1964.

[45] S. Wongwises and W. Kongkiatwanitch, "Interfacial friction factor in vertical upward gas-liquid annular two-phase flow," *Int. Commun. Heat Mass Transf.*, vol. 28, no. 3, pp. 323–336, 2001.

[46] I. Kataoka and M. Ishii, "Mechanism and correlation of droplet entrainment and deposition in annular two-phase flow.[PWR; BWR]," Argonne National Lab., IL (USA), 1982.

[47] B. J. Azzopardi, S. Taylor, and D. B. Gibbons, "Annular two phase flow in a large diameter tube," Harwell, Oxfordshire, UK, 1982.

[48] C. Berna, A. Escrivá, J. L. Muñoz-Cobo, and L. E. Herranz, "Development of new correlations for annular flow," *WIT Trans. Eng. Sci.*, vol. 89, pp. 451–462, 2015.

[49] D. F. Tatterson, J. C. Dallman, and T. J. Hanratty, "Drop sizes in annular gas-liquid flows," *AIChE J.*, vol. 23, no. 1, pp. 68–76, Jan. 1977.

[50] C. Berna, A. Escrivá, J. L. Muñoz-Cobo, and L. E. Herranz, "Review of droplet entrainment in annular flow: Characterization of the entrained droplets," *Prog. Nucl. Energy*, vol. 79, pp. 64–86, 2015.

[51] I. Kataoka, M. Ishii, and K. Mishima, "Generation and Size Distribution of Droplet in Annular Two-Phase Flow," *J. Fluids Eng.*, vol. 105, no. 2, pp. 230–238, Jun. 1983.

[52] B. J. Azzopardi, G. Freeman, and D. J. King, "Drop sizes and deposition in annular two phase flow," Harwel, Oxfordshire, UK, 1980.

[53] A. Al-Sarkhi and T. . Hanratty, "Effect of pipe diameter on the drop size in a horizontal annular gas–liquid flow," *Int. J. Multiph. Flow*, vol. 28, no. 10, pp. 1617–1629, Oct. 2002.

[54] H. Utsuno and F. Kaminaga, "Prediction of Liquid Film Dryout in Two-Phase Annular-Mist Flow in a Uniformly Heated Narrow Tube Development of Analytical Method under BWR Conditions," *J. Nucl. Sci. Technol.*, vol. 35, no. November 2014, pp. 643–653, 1998.

[55] N. Petalas and K. Aziz, "A Mechanistic Model for Multiphase Flow in Pipes," *J. Can. Pet. Technol.*, vol. 39, no. 6, pp. 43–55, Jun. 2000.

[56] H.-Q. Zhang, Q. Wang, C. Sarica, and J. P. Brill, "Unified Model for Gas-Liquid Pipe Flow via Slug Dynamics—Part 1: Model Development," *J. Energy Resour. Technol.*, vol. 125, no. 4, p. 266, Nov. 2003.

[57] P. Sawant, M. Ishii, and M. Mori, "Droplet entrainment correlation in vertical upward co-current annular two-phase flow," *Nucl. Eng. Des.*, vol. 238, no. 6, pp. 1342–1352, Jun. 2008.

[58] P. B. Whalley, G. F. Hewitt, and P. Hutchinson, "Experimental Wave and Entrainment Measurements in Vertical Annular Two-phase Flow," Atomic Energy Research Establishment, Harwell, Oxfordshire, UK, 1973.

[59] D. M. Jepson, B. J. Azzopardi, and P. B. Whalley, "The effect of gas properties on drops in annular flow," *Int. J. Multiph. Flow*, vol. 15, no. 3, pp. 327–339, May 1989.

[60] L. B. Fore and A. E. Dukler, "Droplet deposition and momentum transfer in annular flow," *AIChE J.*, vol. 41, no. 9, pp. 2040–2046, Sep. 1995.

[61] M. B. Alamu, "Investigation of Periodic Structures in Gas-Liquid Flow," University of Nottingham, 2010.

[62] K. Singh, C. C. St. Pierre, W. A. Crago, and E. O. Moeck, "Liquid Film Flow-Rates in Two-Phase Flow of steam and water at 1000 psia.," *AIChe*, vol. 15, no. 1, pp. 51–56, 1969.

[63] J. Wurtz, "An Experimental and Theoretical Investigation of Annular Steam-Water Flow in Tubes and Annuli at 30 to 90 bar," Roskilde, Denmark, 1978.

[64] C. Adamsson and H. Anglart, "Film flow measurements for high-pressure diabatic annular flow in tubes with various axial power distributions," *Nucl. Eng. Des.*, vol. 236, no. 23, pp. 2485–2493, 2006.

[65] H. Langner and F. Mayinger, "Entrainment in Annular Two-Phase Flow under Steady and Transient Flow Conditions," in *Two-Phase Momentum, Heat and Mass Transfer in Chemical, Process, and Energy Engineering Systems, 2*, 1978, pp. 695–706.

[66] T. Ueda and K. K. Kim, "Dryout Heat Flux and Size of Entrained Drops in a Flow Boiling System," *Trans. Japan Soc. Mech. Eng. Ser. B*, vol. 47, no. 418, pp. 1100–1108, 1981.

[67] M. A. Lopez de Bertodano, A. Assad, and S. G. Beus, "Experiments for entrainment rate of droplets in the annular regime," *Int. J. Multiph. Flow*, vol. 27, no. 4, pp. 685–699, Apr. 2001.

[68] G. F. Hewitt and D. N. Roberts, "Studies of Two Phase Patterns by Simultaneous X-Ray and Flash Photography," Harwell, Berkshire, 1969.

[69] Y. Taitel, D. Bornea, and A. E. Dukler, "Modelling flow pattern transitions for steady upward gas-liquid flow in vertical tubes," *AIChE J.*, vol. 26, no. 3, pp. 345–354, May 1980.

[70] M. Shoukri, I. Hassan, and I. Gerges, "Two-Phase Bubbly Flow Structure in Large-Diameter Vertical Pipes," *Can. J. Chem. Eng.*, vol. 81, no. April, pp. 205–211, 2003.

[71] J. P. Schlegel, P. Sawant, S. Paranjape, B. Ozar, T. Hibiki, and M. Ishii, "Void fraction and flow regime in adiabatic upward two-phase flow in large diameter vertical pipes," *Nucl. Eng. Des.*, vol. 239, no. 12, pp. 2864–2874, 2009.

[72] A. Cioncolini and J. R. Thome, "Void fraction prediction in annular two-phase flow," *Int. J. Multiph. Flow*, vol. 43, pp. 72–84, 2012.

[73] A. M. Aliyu, L. Lao, and H. Yeung, "A New Empirical Correlation for Entrained Droplet Fraction Prediction in Co- current Gas – Liquid Annular Two-phase Flow in Large Diameter Pipes 1 Introduction," *APCChE 2015 Congr. Inc. Chemeca 2015*, no. 3131582, pp. 90–101, 2015.

[74] P. Sawant, M. Ishii, T. Hazuku, T. Takamasa, and M. Mori, "Properties of disturbance waves in vertical annular two-phase flow," *Nucl. Eng. Des.*, vol. 238, no. 12, pp. 3528–3541, 2008.

[75] G. B. Wallis, *One Dimensional Two-Phase Flow*, vol. null. New York: McGraw-Hill, 1969.

[76] D. G. Owen, "An experimental and theoretical analysis of equilibrium annular flows," University of Birmingham, 1986.

[77] S. Sugawara, "Droplet deposition and entrainment modeling based on the three-fluid model," *Nucl. Eng. Des.*, vol. 122, no. 1–3, pp. 67–84, 1990.

[78] V. Stevanovic and M. Studovic, "A simple model for vertical annular and horizontal stratified two-phase flows with liquid entrainment and phase transitions: one-dimensional steady state conditions," *Nucl. Eng. Des.*, vol. 154, no. 3, pp. 357–379, 1995.

[79] V. Stevanovic, S. Prica, and B. Maslovaric, "Multi-Fluid Model Predictions of Gas- Liquid

Two-Phase Flows in Vertical Tubes," *FME Trans.*, vol. 35, pp. 173–181, 2007.

[80] V. M. Alipchenkov, R. I. Nigmatulin, S. L. Soloviev, O. G. Stonik, L. I. Zaichik, and Y. A. Zeigarnik, "A three-fluid model of two-phase dispersed-annular flow," *Int. J. Heat Mass Transf.*, vol. 47, no. 24, pp. 5323–5338, 2004.

Figures

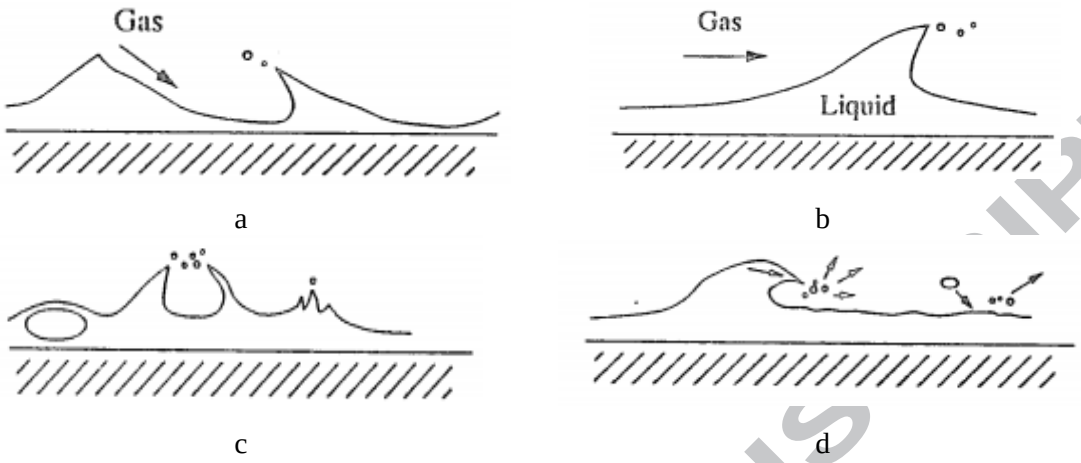

Figure 1: Entrainment mechanisms. (a) Roll wave, (b) Wave undercutting, (c) Bubble burst, (d) Liquid impingement [17]

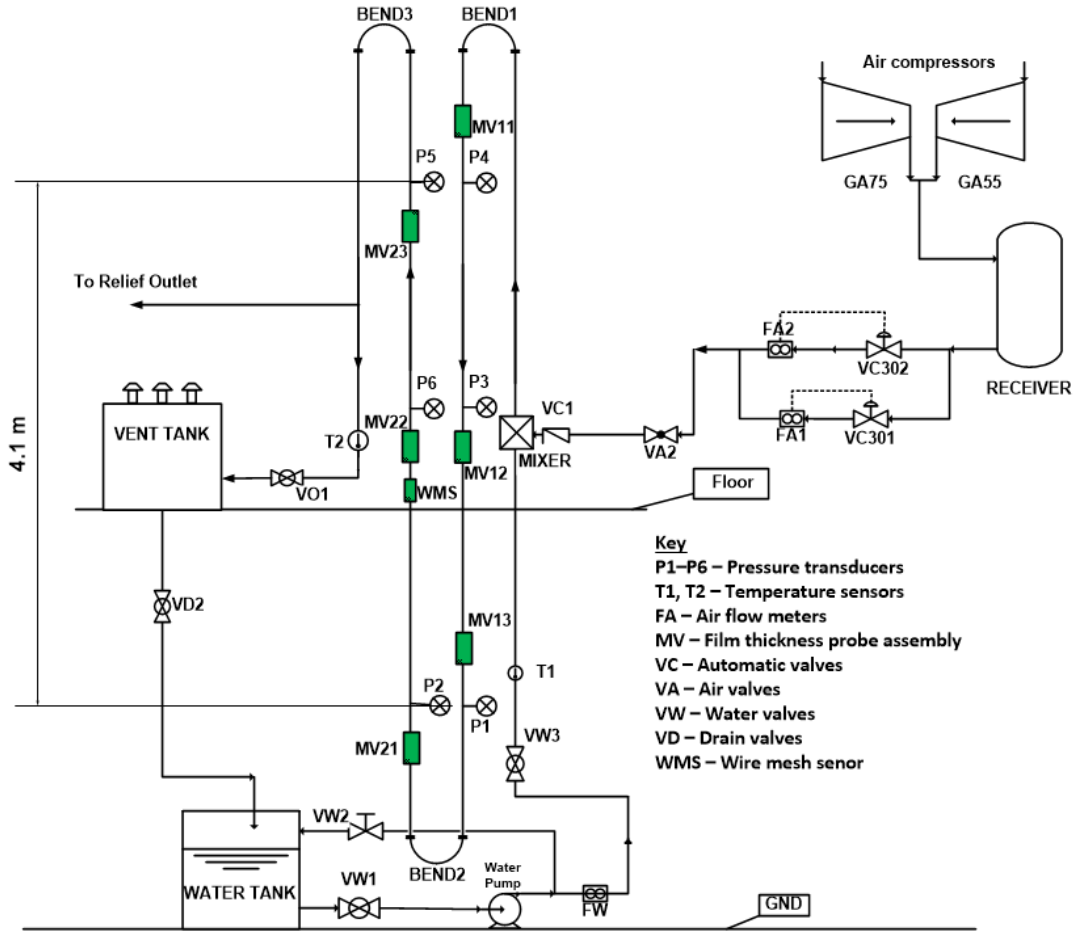

(a)

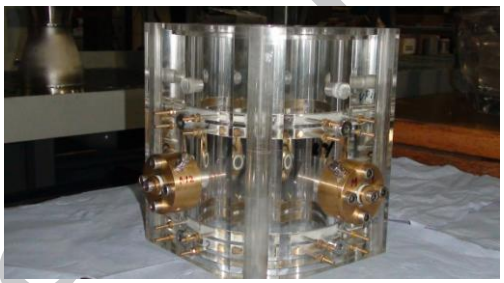

(b)

(c)

Figure 2: (a) Cranfield University's air-water Serpent Rig experimental facility, (b) Integrated conductance film thickness probe spool with electrolyte injection for film velocity determination, (c) Void fraction capacitance Wire Mesh Sensor (WMS)

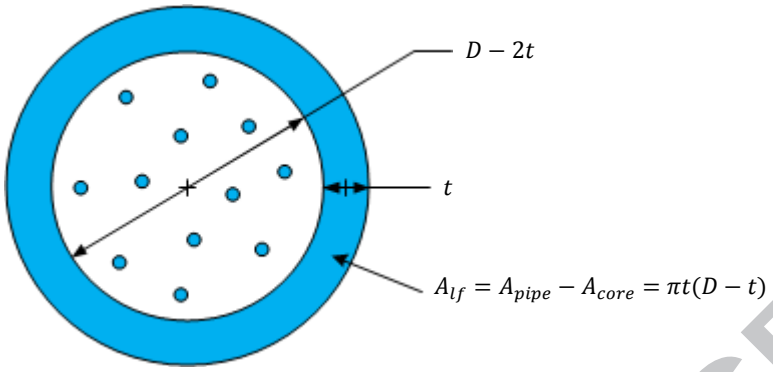

Figure 3: Schematic for liquid mass balance showing the film and droplets as they occupy the pipe cross-section

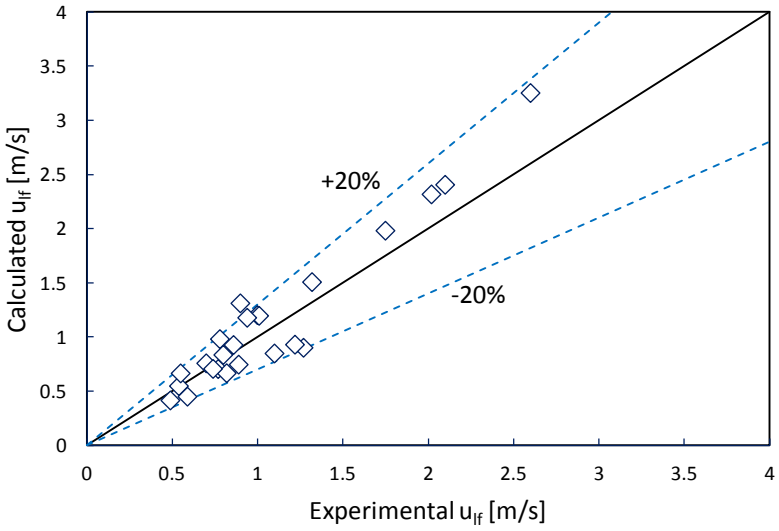

Figure 4: Comparison of experimental liquid film velocity with that calculated using the mass balance Eq. 10

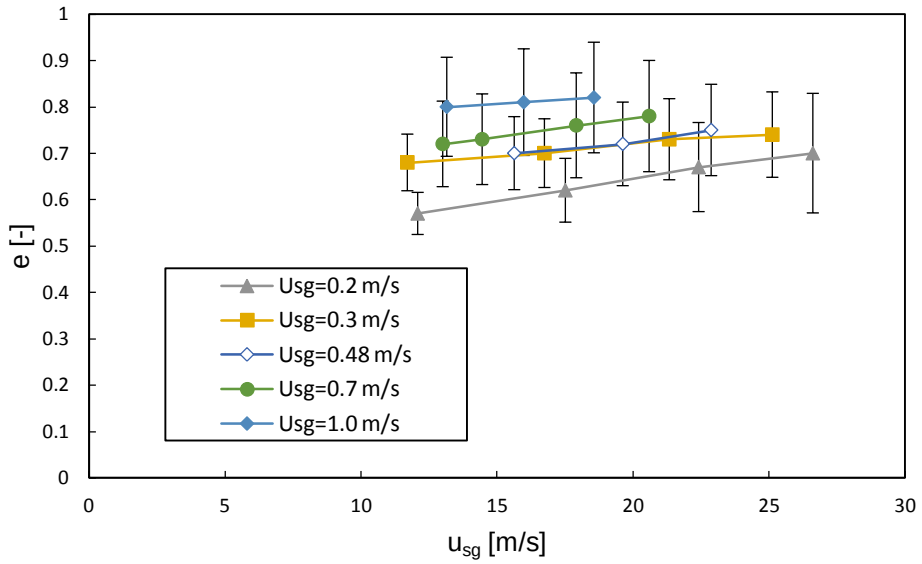

Figure 5: Variation of experimental entrained droplet fraction in with gas flow. Error bars indicate uncertainties propagated from full-scale measurement uncertainties calculated using Eq. 12.

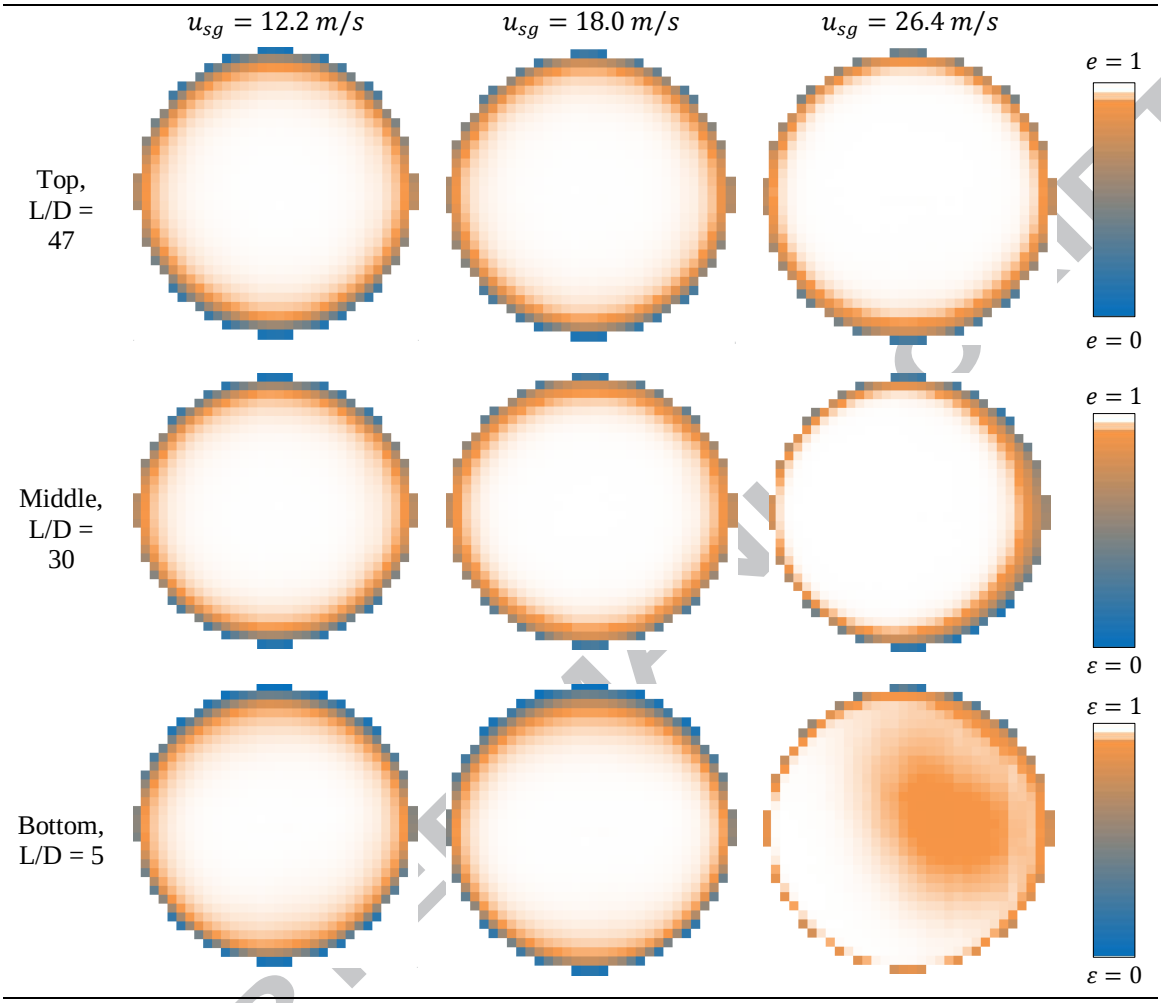

(a)

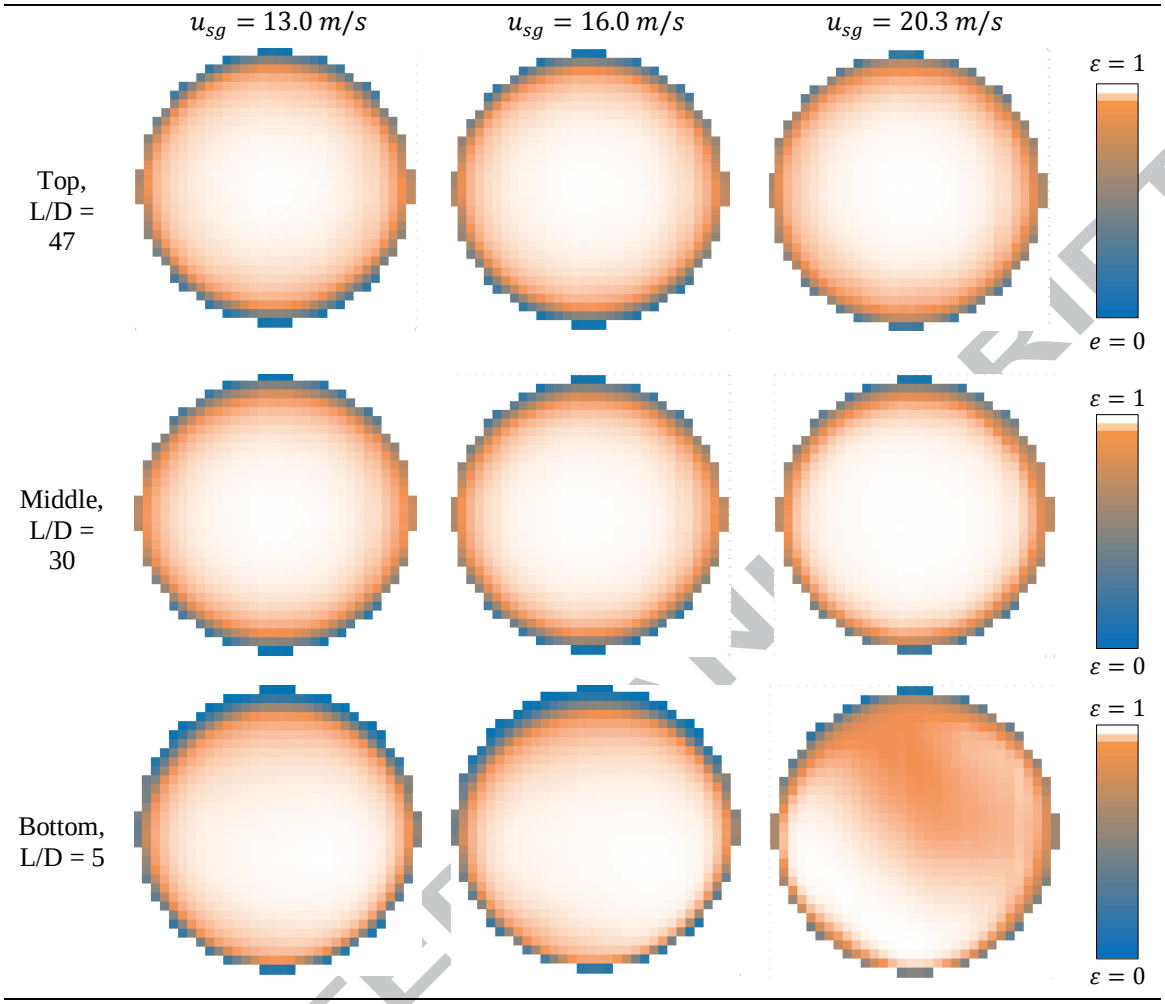

(b)

Figure 6: Sample reconstructed time-averaged WMS images for upward flow at (a) $u_{sl} = 0.30\ m/s$ (top), and (b) $u_{sl} = 1.0\ m/s$ (bottom). Taken at L/D = 5, 30, and 47 from BEND2. Blue indicates water at low void fraction (ε) values, white indicates air at $\varepsilon \rightarrow 1$, and orange indicates entrained liquid droplets at intermediate ε values.

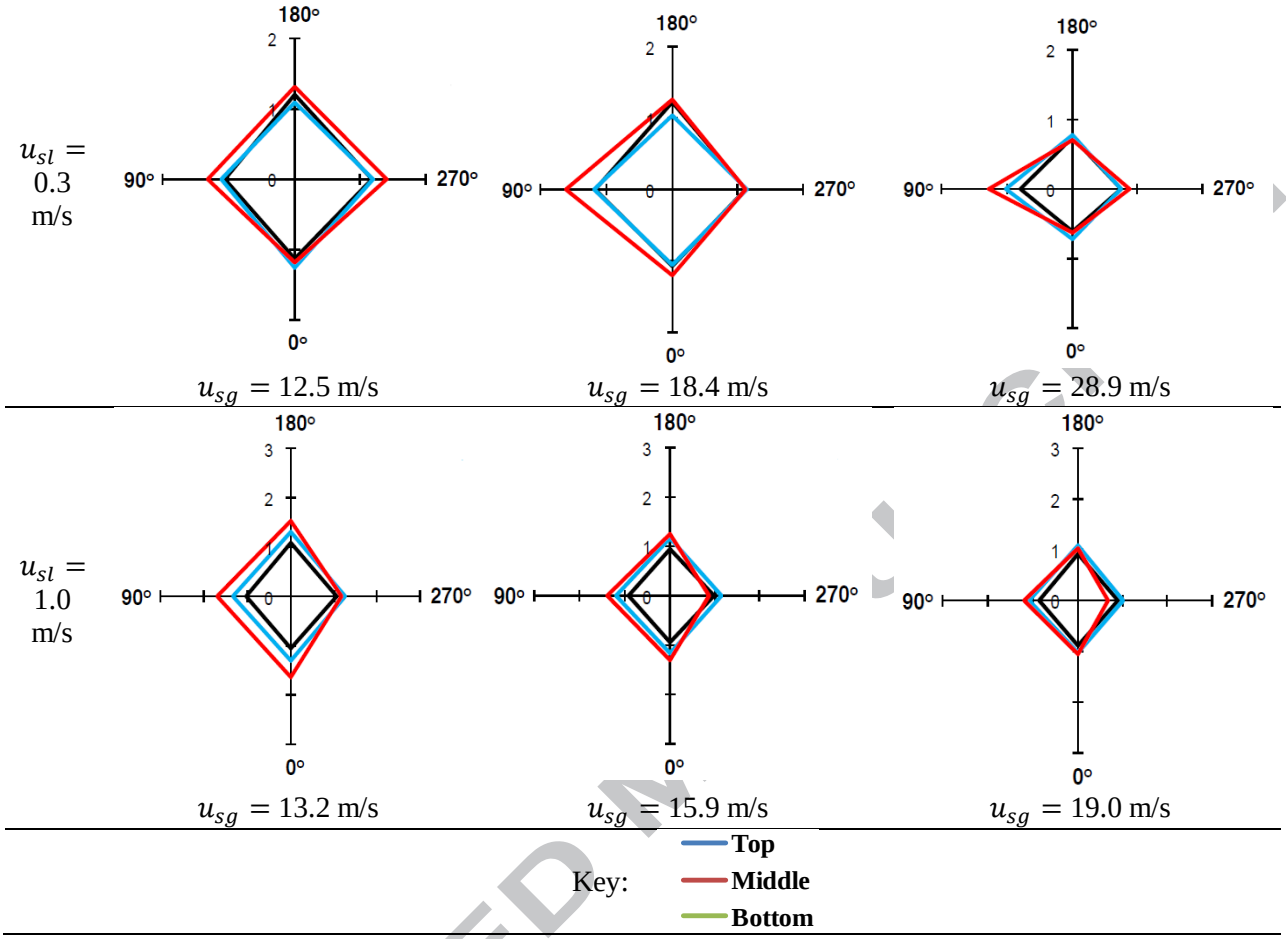

Figure 7: Radar plots showing the effects of gas and liquid superficial velocities on circumferential film thickness variation at the top, middle, and bottom axial positions (u_{sl} = 0.1 m/s; all axis units in mm).

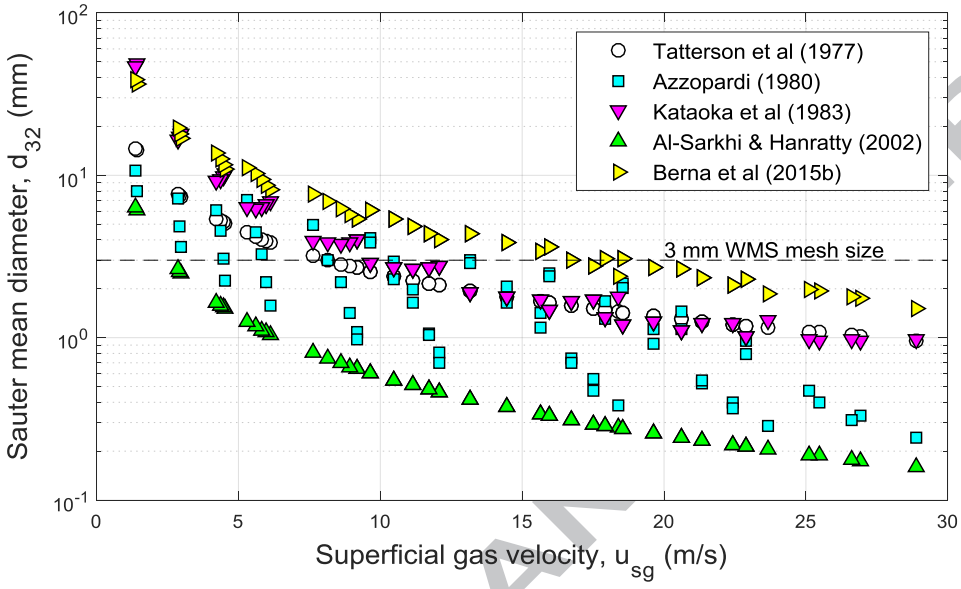

Figure 8: Droplet size estimation using various correlations

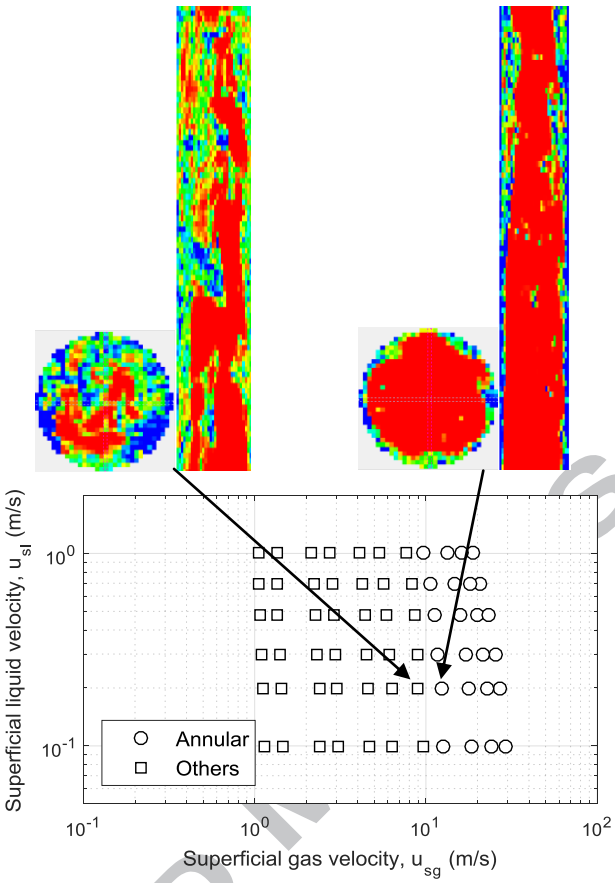

(a)

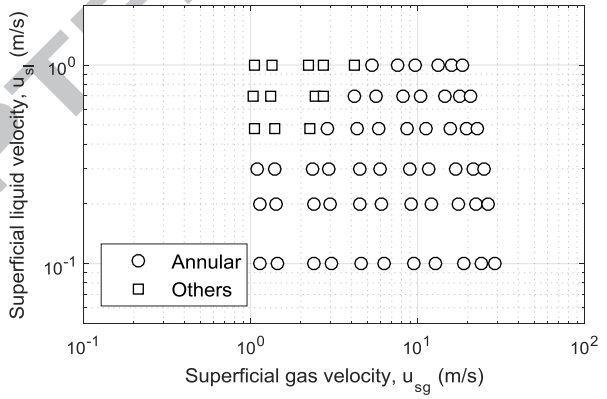

(b)

Figure 9: Flow regime maps obtained for (a) upward (see Aliyu et al. [54]**) and (b) downward flow. . Snapshots of videos produced using stacked WMS images of flow at u_{sl} = 0.2 m/s were used to differentiate between churn and annular flows at u_{sl} = 9.7, and 14.1 m/s respectively**

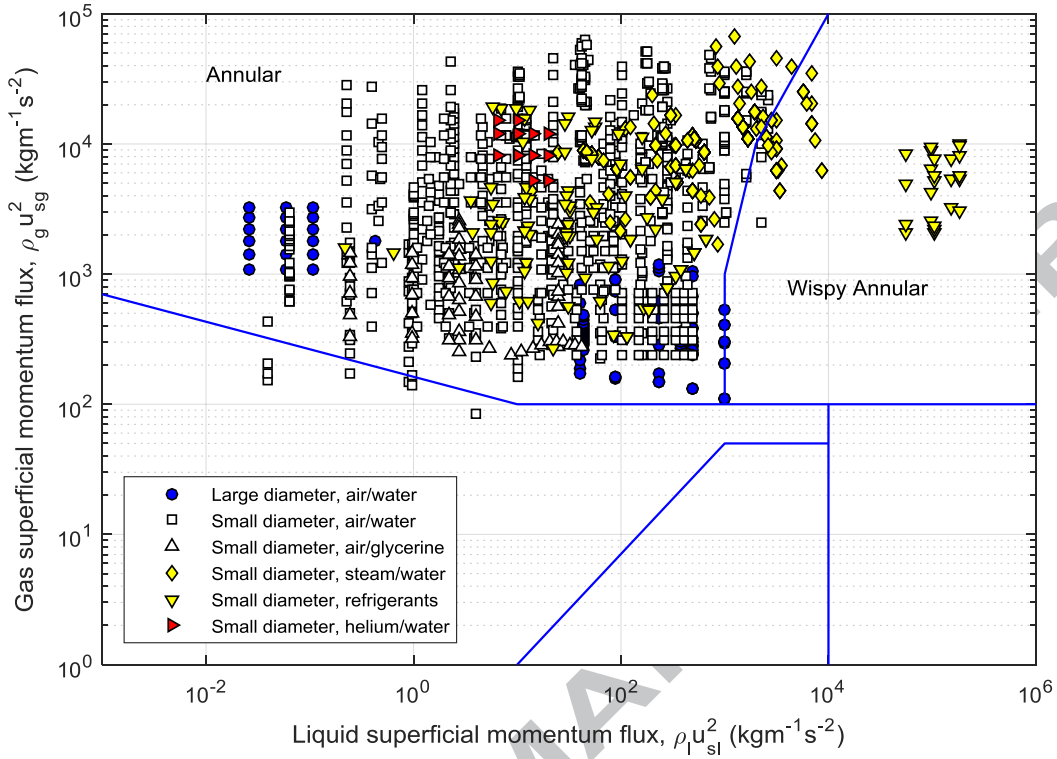

(a)

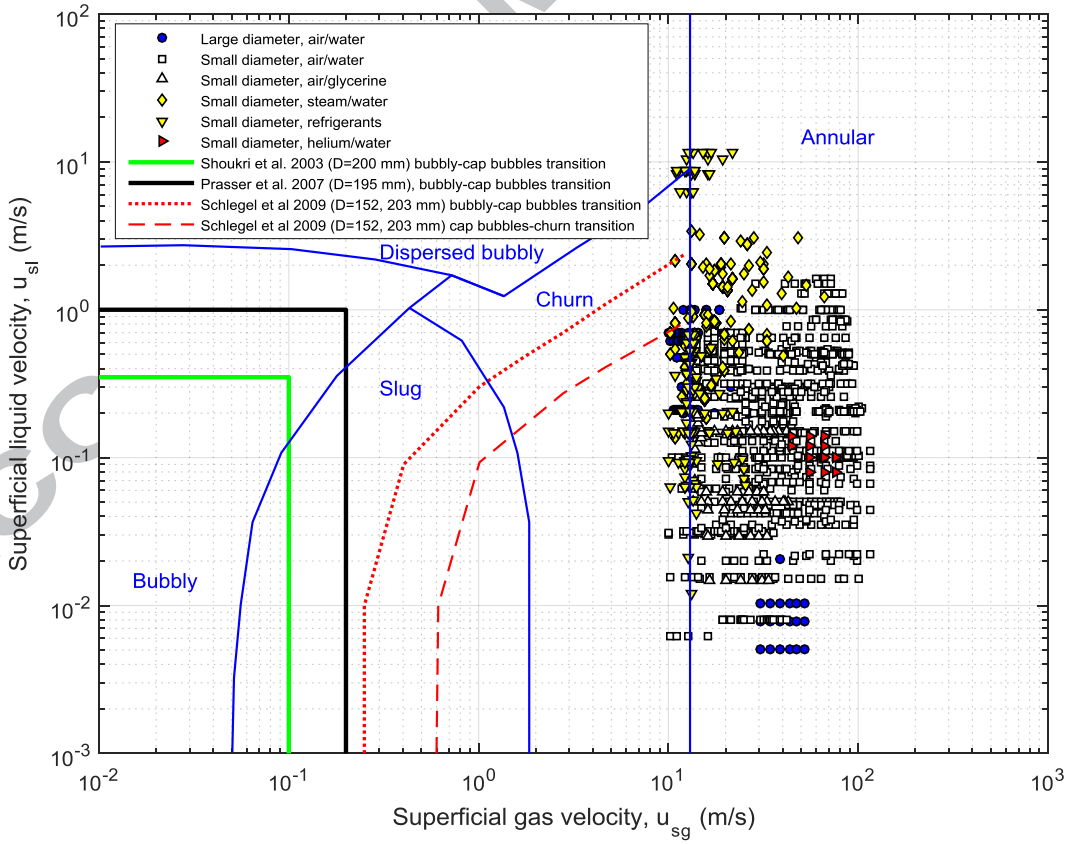

(b)

Figure 10: Flow conditions for the entire database plotted on the (a) Hewitt and Roberts' [65] flow regime map, and (b) Taitel et al [66] including flow regime transitions observed in 152–203-mm by other authors. Blue lines and text are the regimes/transitions determined by Taitel et al.'s criteria.

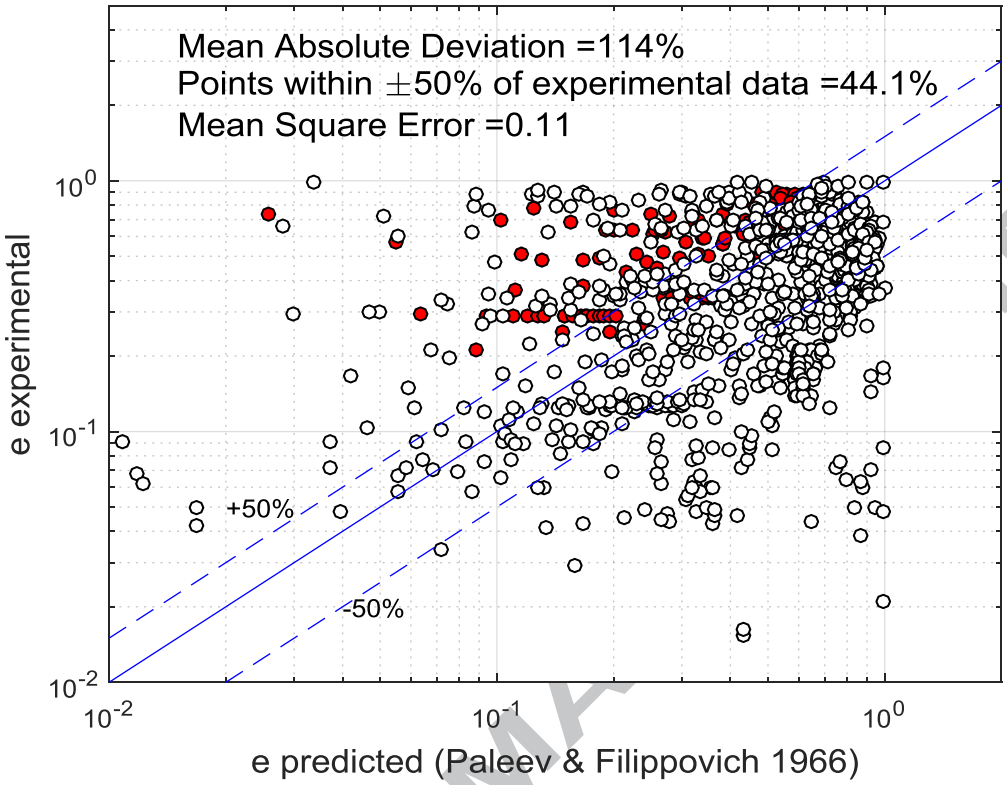

(a)

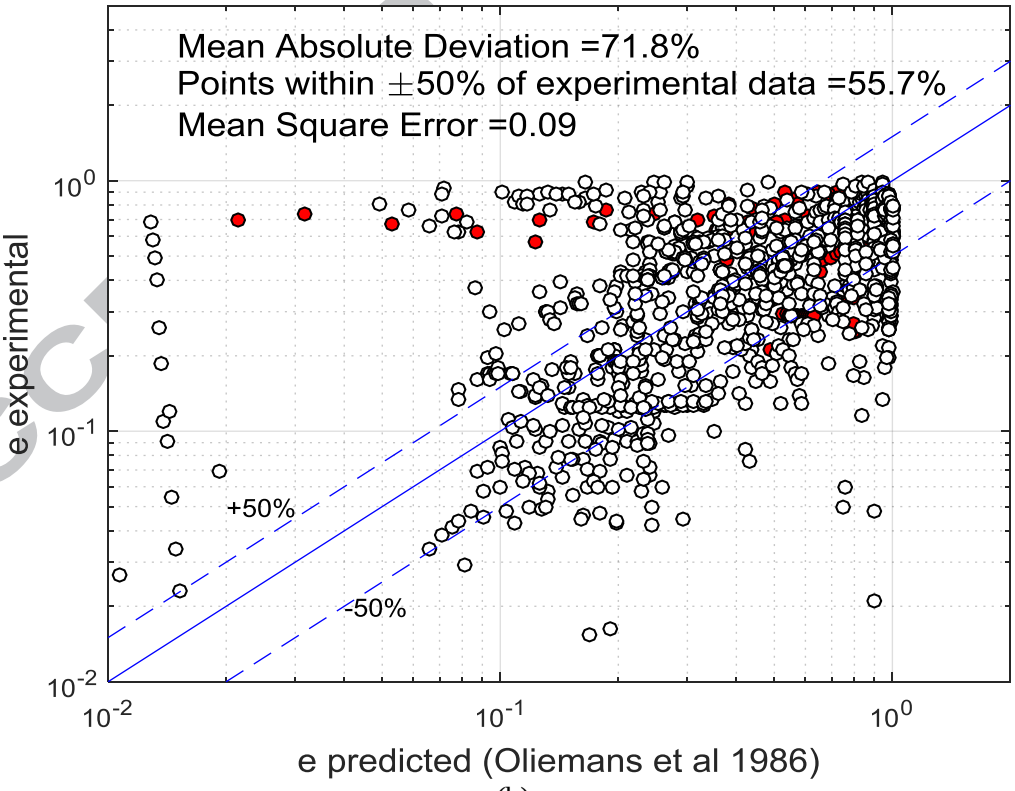

(b)

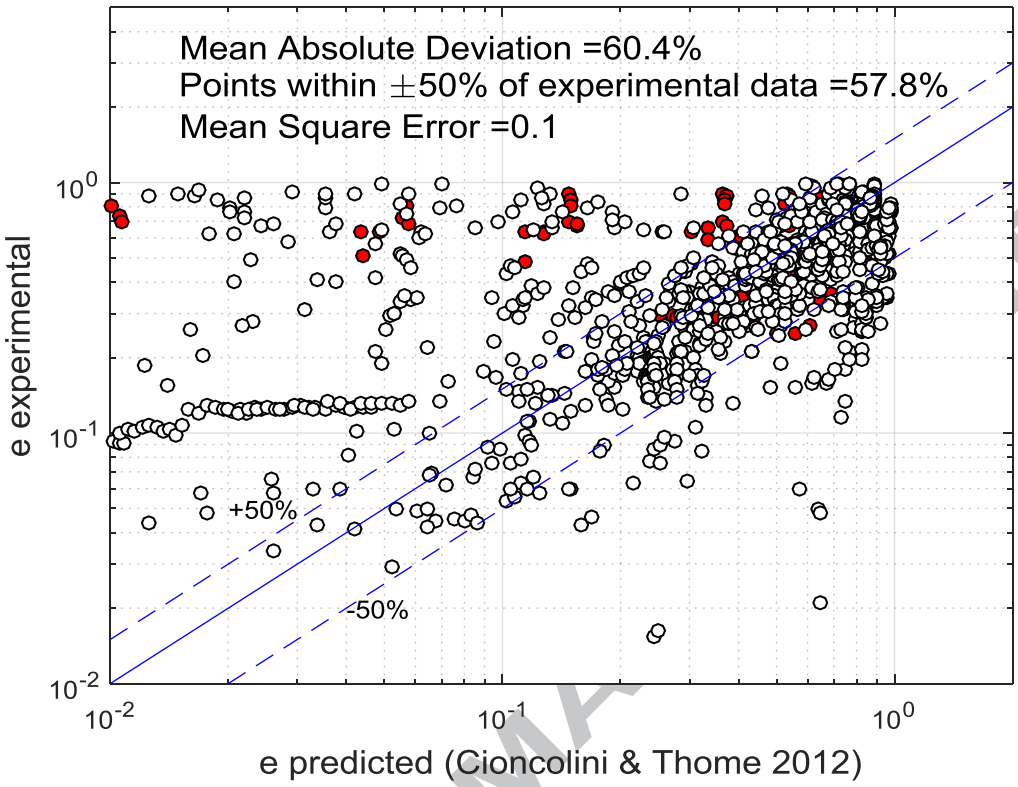

(c)

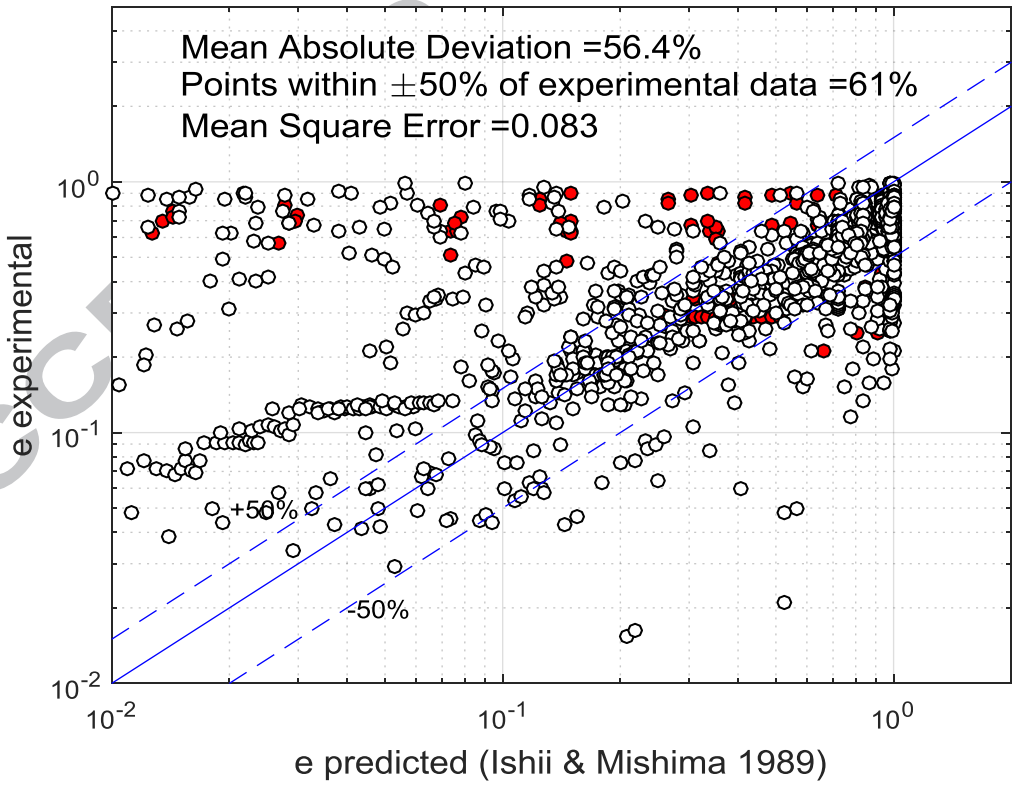

(d)

Figure 11: Comparison of experimental data with selected published correlations for entrained droplet fraction. Coloured points indicate data from large-diameter pipes.

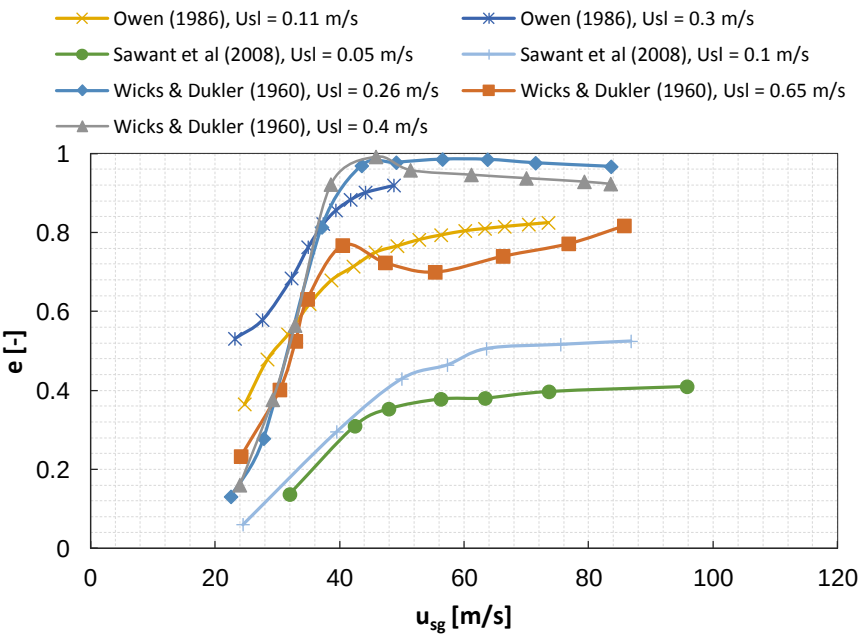

Figure 12: Effect of gas velocity on entrained droplet fraction

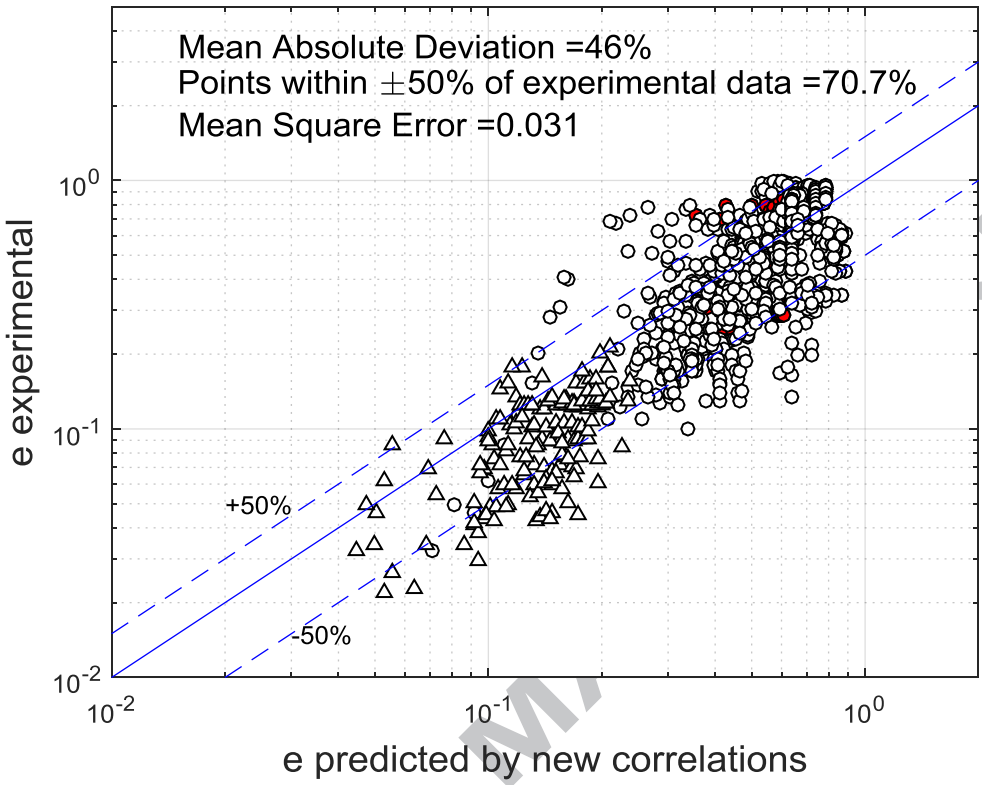

Figure 13: Comparison of experimental entrained droplet fraction values with predictions by Eq. 30 (circles) and 31 (triangles)

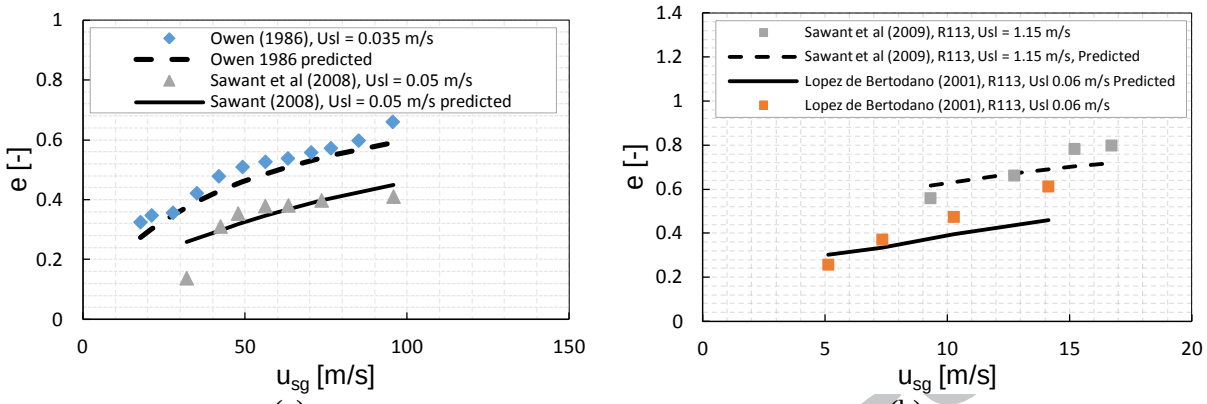

Figure 14: Comparison between predictions and selected data: (a) air/water experimental data [73], [74] **showing the effect of superficial gas velocity, (b) R113 data** [27], [63]

Tables

Table 1: Parameters obtained by different authors for Eq. (14)

Correlation	*K*	*a*	*b*	*c*	*d*	*e*
Tatterson et al. [68]	0.106	-	0.100	-0.500	-	-
Kataoka et al. [70]	0.028	0.667	-0.167	-1.000	-0.333	0.667
Berna et al. [67]	2.634	-0.540	0.130	-0.23	-	-

Table 2: Experimental database gathered for this study

S/No.	Author(s)	Fluid combination	D (mm)	L/D	Test pressure (bara)	u_{sl} range (m/s)	u_{sg} range (m/s)	Number of data points
A.	Small diameter							
1	Wicks and Dukler [3]	Air/water	28.58	245	1.2	0.13–0.78	22–89	54
2	Wallis [4]	Air/water	12.7	n/a	1.0	0.042–0.168	20–45	41
3	Cousins and Hewitt [5]	Air/water	32	480	1.2–4.0	0.008–0.01	19–42	40
4	Singh et al. [6]	Steam/water	12.5	180	69–83	0.18–0.9	8–16	15
5	Andreussi and Zanelli [7]	Air/water	24	n/a	1.2	0.37–2.95	5–70	9
6	Wurtz [8]	Steam/water	17	450–900	30–90	0.26–3.0	10–67	122
7	Langner and Mayinger [9]	R12	14	357	11.0	0.01–0.38	2.3–6.8	20
8	Ueda and Kim [10]	R113	10	245	3.3	0.23–0.68	4–17	27
9	Andreussi [11]	Air/water	24	208	1.5	0.02–0.44	39–68	33
10	Owen [12]	Air/water	32	600	2.0–4.0	0.02–1.00	14–100	97
11	Zabaras et al [13]	Air/water	50.8	90	1.7	0.006–0.06	9 –27	26
12	Jepson et al. [14]	Air/water, helium/water	10.26	292	1.5	0.08–0.14	33–67, 44–76	27
13	Schadel et al. [15]	Air/water	25	150	1.2	0.18–1.04	32–116	32
14	Fore and Dukler [16]	Air/glycerine	50.8	69	1.0	0.006–0.06	16–36	65
15	Lopez de Bertodano et al. [17]	Air/water	10	420	2.8	0.74–0.54	25–126	20
16	Lopez de Bertodano et al. [18]	R113	10	350	1.4–6.6	0.1–0.35	4–25	48
17	Azzopardi and Zaidi [19]	Water/air	38	118	1.5	0.02–0.1	15–30	28
18	Feldhaus et al. [20]	Air/water	9.35	241	2.8	0.3–0.65	36–86	14
19	Pan and Hanratty [21]	Air/water	25.4	n/a	1.2	0.04–0.08	32–116	10
20	Okawa et al. [22]	Air/water	5	320	1.4–7.6	0.1–1.6	20–105	170
21	Adamson and Anglart [23]	Steam/water	14	194–261	70	0.28–1.5	15–20	153
22	Kaji and Azzopardi [24]	Air/water	19	300	1.2	0.03–0.65	10–34	32
23	Alamu [25]	Air/glycerine	5	390	1.5	0.05–0.19	13–43	37
24	Sawant et al. [26]	Air/water	9.4	210	1.2– 4.0	0.05–0.5	16–95	77
25	Sawant et al. [27]	R113	10.2	400	2.8–8.5	0.87 – 1.0	9–22	24
26	Al-Yarubi [28]	Air/water	15	40	1.0			70
B.	Large diameter							
27	Azzopardi et al. [29]	Air/water	125	40	1.0	0.005–0.02	30–52	19
28	Van der Meulen [30]	Air/water	127	87	2.0	0.02–0.70	10–17	31
29	Current	Air/water	101.6	47	1.0–1.4	0.1-1.0	10–29	26
	Total							1,391

Table 3: Summary of correlations used to compare with experimental database

S/No.	Reference	Correlation	Notes
1	Paleev and Filippovich [4]	$e = 0.015 + 0.44\log\left[\frac{\bar{\rho}}{\rho_L}\left(\frac{\mu_L u_{sg}}{\sigma}\right)^2 \times 10^4\right]$ where $\bar{\rho} = \rho_g\left[1 + \frac{e(1-x)}{x}\right]$. As can be seen, the solution for e requires an iterative procedure.	The best predictions when compared to the current database were for e > 0.6. Nevertheless, many e values were greater than 1
2	Wallis [5]	Same form as [4] except for the use of ρ_g instead of $\bar{\rho}$, thereby avoiding an iterative solution.	Produced slightly less scatter than correlation 1, but large errors still occur at e < 0.5
3	Oliemans et al. [6]	$\frac{e}{(1-e)} = 10^{\beta_0}\rho_l^{\beta_1}\rho_g^{\beta_2}\mu_l^{\beta_3}\mu_g^{\beta_4}\sigma^{\beta_5}D^{\beta_6}u_{sl}^{\beta_7}u_{sg}^{\beta_8}g^{\beta_9}$, where $\beta_0 - \beta_9$ are regression constants that depend on film Reynolds number ranges given in Table 4. Iterative.	Developed for vertical upflows using the Harwell Databank consisting of air/water, steam, and hydrocarbon flows. Pressures of 1–100 bar. Pipe diameters of 9.3–31.8 mm. 727 data points.
4	Ishii and Mishima [21]	$e = \tanh\left(7.25 \times 10^{-7} We^{1.25} Re_l^{0.25}\right)$	Air/water vertical up and down-flows in pipes of 9.5 – 15.6 mm. Pressures of 1–2.7 bar.
5	Hewitt and Govan [7]	$e = 5.75 \times 10^{-5}\frac{x}{1-x}\left[(\dot{m}_{lf} - \dot{m}_{lfc})^2\frac{D\rho_L}{\sigma\rho_g^2}\right]^{0.316}$ for $\dot{m}_{lf} > \dot{m}_{lfc}$ where $\dot{m}_{lf}$ is correlated by $\dot{m}_{lf} = \frac{\mu_L}{D}\exp\left(5.8504 + 0.4249\frac{\mu_g}{\mu_l}\sqrt{\frac{\rho_l}{\rho_g}}\right)$ to avoid an iterative procedure.	Obtained for non-equilibrium flows using data from the Harwell Databank for steam/water, air/water, air/genklene, and fluoroheptane flows.
6	Utsono and Kaminanga [54]	$e = \tanh\left(0.16 We_g^{0.08} Re_l^{0.16} - 1.2\right)$	Developed from steam/water data only at 30–90 bar. Gives negative values at low entrained fractions for other data.
7	Petalas and Aziz [55]	$\frac{e}{1-e} = 0.735\left(\frac{\mu_l^2 u_{sg}^2 \rho_g}{\sigma^2 \rho_l}\right)^{0.074}\left(\frac{u_{sl}}{u_{sg}}\right)^{0.2}$	Unable to predict *e* less than 0.5, most predictions clustered above 0.8 with many large deviations.
8	Pan and Hanratty [8]	$\frac{e/e_M}{1-e/e_M} = 6 \times 10^{-5}(u_{gc} - u_{sg})^2(\rho_g\rho_l)^{0.5}D/\sigma$ where $e_M = 1 - \dot{m}_{lfc}/\dot{m}_{lf}$	Air/water, Freon/Freon, helium/water, air/genklene flows. Pipes of 10.6 – 57.1 mm,
9	Barbosa et al. [11]	$e = 0.95 + 342.5\sqrt{\frac{\rho_l \dot{m}_l}{\rho_g \dot{m}_g}}D^2$ for $0.9 < U_g^* < 1.3$	Air/water experimental data in a 31.8-mm pipe for 1.3 – 5 bar.
10	Zhang et al. [56]	$\frac{e}{1-e} = 0.003 We^{1.8} Fr_g^{-0.92} Re_l^{0.7} Re_g^{-1.24}\left(\frac{\rho_l}{\rho_g}\right)^{0.38}\left(\frac{\mu_l}{\mu_g}\right)^{0.97}$	Developed as a rearrangement of [6] into dimensionless form, but it produced consistently small *e* values
11	Sawant et al.[57]	$e = e_m \tanh\left(2.31 \times 10^{-4} Re_l^{-0.35} We^{1.25}\right)$ where $e_m = 1 - Re_{lf,lim}/Re_l$ and $Re_{lf,lim} = 250\ln(Re_l) - 1265$	Air/water data in 9.4-mm pipe. Pressures of 1.2 –4 bar
12	Sawant et al. [27]	$e = \left(1 - \frac{13N_{\mu l}^{-0.5} + 0.3\left(Re_l - N_{\mu l}^{-0.5}\right)^{0.95}}{Re_l}\right) \times \tanh\left[2.31 \times 10^{-4} Re_l^{-0.35}(We - We_{cr})^{1.25}\right]$ where $N_{\mu l} = \mu_l\Big/\left(\rho_l\sigma\sqrt{\frac{\sigma}{g\Delta\rho}}\right)^{1/2}$	Air/water and R113 in 9.4 and 10.2-mm pipes, respectively. Pressures of 1.2 – 8.5 bar .
13	Cioncolini and Thome [9]	$e = (1 + 13.18 We_c^{-0.655})^{-10.77}$ where $W_c = \frac{\rho_c u_c^2 D_c}{\sigma}$, $\rho_c = (1-\varepsilon_c)\rho_l + \varepsilon_c\rho_g$, $\varepsilon_c =$	Air/water, helium/water, air/genklene, steam/water, Freon flows, pipe diameters of 5 to 57

		$\frac{\varepsilon}{1+\gamma(1-\varepsilon)}$, $\gamma = e\frac{\varepsilon}{1-\varepsilon}\frac{1-x}{x}\frac{\rho_g}{\rho_l}$ and $u_c = \frac{[x+e(1-x)]\dot{m}_t}{\rho_c}\left(\frac{D}{D_c}\right)^2$. Correlation is iterative, requiring an initial estimate of the core velocity in a predictor–corrector approach.	mm, downward and horizontal flows included, 1504 data points
14	Cioncolini and Thome [10]	$e = (1 + 279.6We_c^{-0.8395})^{-2.209}$ where $We_c = \frac{\rho_c u_{sg}^2 D}{\sigma}$	Same as above but diabatic flows included. Pipe diameters of 5 to 95 mm, 2293 data points. However, many data points deemed outliers were "cleaned".
15	Berna et al. [50]	$\frac{e}{1-e} = 5.51 \times 10^{-7} We_g^{2.68} Re_l^{0.34} Re_g^{-2.62} \left(\frac{\rho_l}{\rho_g}\right)^{0.37} \left(\frac{\mu_l}{\mu_g}\right)^{3.71} C_w^{4.24}$, where $C_w = 0.028 N_\mu^{-0.8}$ for $N_\mu \leq \frac{1}{15}$ $C_w = 0.25$ for $N_\mu > \frac{1}{15}$, $N_\mu = \mu_l / \left(\rho_l \sigma \sqrt{\frac{\sigma}{g\Delta\rho}}\right)^{1/2}$	Cannot predict large entrainment values due to their dataset mostly in the region of $e < 0.3$. Even so, the predictions produced an inverse trend for many data points and gave large deviations for $e > 0.1$

Table 4: Parameters for the Oliemans et al. [6] correlation.

Re_{lf}	β_0	β_1	β_2	β_3	β_4	β_5	β_6	β_7	β_8	β_9
All values	-2.52	1.08	0.18	0.27	0.28	-1.80	1.72	0.70	1.44	0.46
10^2-3×10^2	-0.69	0.63	0.96	-0.80	0.09	-0.88	2.45	0.91	-0.16	0.86
3×10^2-10^3	-1.73	0.94	0.62	-0.63	0.50	-1.42	2.04	1.05	0.96	0.48
10^3-3×10^3	-3.31	1.15	0.40	-1.02	0.46	-1.00	1.97	0.95	0.78	0.41
3×10^3-10^4	-8.27	0.77	0.71	-0.13	-1.18	-0.17	1.16	0.83	1.45	-0.32
10^4-3×10^4	-6.38	0.89	0.70	-0.17	-0.55	-0.87	1.67	1.04	1.27	0.07
3×10^4-10^5	-0.12	0.45	0.25	0.86	-0.05	-1.51	0.91	1.08	0.71	0.21

Highlights

- Experiments conducted for gas–liquid flow in a large diameter flow loop.
- Data were collected for the entrained droplet fraction in the annular flow regime.
- Droplet fraction data were gathered from other sources for both small and large pipes.
- Correlation derived using over 1,300-point database for entrained droplet fraction.